

Thesis Title

Thomas P. Ogden

Abstract

Here is my abstract.

Thesis Title

Thomas P. Ogden

A thesis submitted in partial fulfilment
of the requirements for the degree of
Doctor of Philosophy.



Department of Physics
Durham University

January 3, 2016

Declaration

I confirm that no part of the material offered has previously been submitted by myself for a degree in this or any other University. Where material has been generated through joint work, the work of others has been indicated.

Thomas P. Ogden

Durham, January 3, 2016

The copyright of this thesis rests with the author. No quotation from it should be published without their prior written consent and information derived from it should be acknowledged.

*Dedicated to Someone Special,
for some special reason.*

Contents

1	Introduction	9
2	Propagation of Light in Thermal Atomic Vapours	10
2.1	Introduction	10
2.2	Deriving the Propagation Equation	10
2.2.1	Maxwell's Equations and the Wave Equation	11
2.2.2	The Slowly Varying Envelope Approximation	13
2.2.3	Energy and Intensity	15
2.3	Linear Optics, Susceptibility and Refractive Index	15
2.3.1	Susceptibility	15
2.3.2	Refractive Index	18
2.4	Interaction of Light with Atoms	19
2.4.1	Spontaneous Decay of Excited States	20
2.4.2	The Interaction Hamiltonian	20
2.4.3	Dipole Matrix Elements and Parity	22
2.4.4	Atomic Coherence and Polarisation	23
2.4.5	Thermal Atoms	24

2.4.6	Shifting to the Speed-of-Light Reference Frame	25
2.4.7	A Recap	25
2.5	Linear Propagation in Two-level Atoms	26
2.5.1	The Two-level System	27
2.5.2	The Natural Unit System	28
2.5.3	Weak Probe Lineshape	29
2.5.4	Weak Pulse Propagation Results	30
2.5.5	Spectral Analysis	33
2.5.6	The Voigt Profile	39
2.6	Discussion	41
3	Nonlinear Propagation Phenomena	43
4	Storage and Retrieval of Dark-State Polaritons	44
5	Two-Photon Excitation in a High-Intensity Beam	45
6	Propagation of Short Pulses in V-type Atoms	46
6.1	Introduction	46
6.2	Description of the Experiment	47
6.2.1	Experimental Results	49
6.3	Theoretical Model	51
6.3.1	Simulation Results	53
6.3.2	Inhomogeneous Broadening	58
6.3.3	Collision Dephasing	59

6.3.4	Hyperfine Pumping	60
6.4	Comparison of Simulation Results with Data	62
6.4.1	Power Dependence	64
6.4.2	Temperature Dependence	66
6.4.3	A Recap	68
6.5	Analysis of the Evolution of a Single Atom	68
6.5.1	Coherent Population Trapping	71
6.6	Simulating Longer Propagation Distances	74
6.6.1	Propagation in the Coupling Pulse Scheme	74
6.6.2	Comparison with Experimental Data	78
6.6.3	Hyperfine Structure & Degeneracy	80
6.6.4	Weak Probe Fields	82
6.7	Discussion	83
7	Conclusions	88
A	Dynamics of Open Quantum Systems	89
A.1	The Density Operator	89
A.2	The Master Equation	91
B	Numerical Integration of the Lindblad Master Equation	93
C	Numerical Integration of the Maxwell-Bloch Equations	94
C.1	Formulating the Problem	94
C.2	Computational Scheme	96

C.2.1 Details of the Algorithm	98
C.2.2 Code Implementation	99
C.3 Convergence & Accuracy	99
C.4 Parallelisation & Performance	103
D The Two-Step Adams-Bashforth Method	106
Acknowledgements	109
Bibliography	110

1 Introduction

2 Propagation of Light in Thermal Atomic Vapours

2.1 Introduction

In this chapter we will define the model for propagation in thermal atoms to be used throughout the thesis, based on the well-known Maxwell Bloch (MB) equations. We will introduce the concept of susceptibilities and discuss analytic solutions to the equations that are available in the regime of weak incident light, before generalising the problem to nonlinear interaction with quantised atoms. Finally we will present results from numerical solutions and compare with the analytic results for weak fields to verify the accuracy of the numerical model.

2.2 Deriving the Propagation Equation

In this section we will derive an equation to describe the propagation of a classical electromagnetic field in a polarised medium. Our starting point, naturally, is Maxwell's set of equations of classical electrodynamics.

2.2.1 Maxwell's Equations and the Wave Equation

In a medium with no free charges or free current, Maxwell's equations for the electric field \mathbf{E} and the magnetic field \mathbf{B} can be written¹

$$\nabla \cdot \mathbf{D} = 0 \quad (2.1a)$$

$$\nabla \cdot \mathbf{B} = 0 \quad (2.1b)$$

$$\nabla \times \mathbf{E} = -\frac{\partial \mathbf{B}}{\partial t} \quad (2.1c)$$

$$\nabla \times \mathbf{B} = \mu_0 \frac{\partial \mathbf{D}}{\partial t}. \quad (2.1d)$$

The electric displacement \mathbf{D} accounts for the effect of charges in a medium and is given by

$$\mathbf{D} = \epsilon_0 \mathbf{E} + \mathbf{P} \quad (2.2)$$

where ϵ_0 is the vacuum permittivity and the electric polarisation \mathbf{P} describes the cumulative effect of induced dipole moments in individual atoms. We'll discuss the source of polarisation in atoms further in section 2.3.

Taking the curl of (2.1c) and substituting (2.1d) we find

$$\nabla \times (\nabla \times \mathbf{E}) = -\mu_0 \frac{\partial \mathbf{D}^2}{\partial t^2}.$$

We then apply the vector identity

$$\nabla \times (\nabla \times \mathbf{E}) = \nabla(\nabla \cdot \mathbf{E}) - \nabla^2 \mathbf{E}$$

and, assuming that the polarisation varies little in the plane transverse to propagation such that $\nabla \cdot \mathbf{P} \approx 0$, arrive at the Maxwell wave equation

$$\nabla^2 \mathbf{E} - \frac{1}{c^2} \frac{\partial^2 \mathbf{E}}{\partial t^2} = \mu_0 \frac{\partial^2 \mathbf{P}}{\partial t^2}. \quad (2.3)$$

The Maxwell wave equation (MWE) thus describes the wave-like propagation of an electric field \mathbf{E} through a medium with polarisation \mathbf{P} . The

second derivative on the right-hand side tells us that the accelerating charges described by \mathbf{P} can act as a source of new components of the electromagnetic field. For this reason, polarisation plays a critical role in practically all optical phenomena.²

A similar propagation equation to (2.3) may be derived for the magnetic field, however we'll find that the interaction of atoms with the electric field dominates and so we will not consider \mathbf{B} further.

We will consider 1D propagation along the z -axis, a restriction well-justified by the deconstructive interference of light scattered by atomic dipoles in directions not aligned with the incident radiation.³ Then we might write the transverse field as $\mathbf{E} = \hat{\mathbf{x}}E(z, t)$, where $\hat{\mathbf{x}}$ is a unit vector perpendicular to z . We assume that we are dealing with atoms that are electrically neutral to start with, such that all of the polarisation in the medium will be induced by that field, so we may similarly set $\mathbf{P} = \hat{\mathbf{x}}P(z, t)$. In this way we can reduce the MWE to the scalar form

$$\frac{\partial^2 E}{\partial z^2} - \frac{1}{c^2} \frac{\partial^2 E}{\partial t^2} = \mu_0 \frac{\partial^2 P}{\partial t^2}. \quad (2.4)$$

In the absence of sources (i.e. $P = 0$) we can solve the homogeneous equation (2.4) analytically. For a nonconducting medium with spatially constant permeability and susceptibility the solution is a transverse monochromatic plane wave¹

$$\tilde{E}(z, t) = \tilde{E}_0 e^{i(kz - \omega t)}. \quad (2.5)$$

where as usual k represents wavenumber and ω the angular frequency. The amplitude is given by \tilde{E}_0 . Of course, the electric field is an observable physical quantity and so must be real-valued — it is the real part of the complex $\tilde{E}(z, t)$ given by

$$E(z, t) = \Re[\tilde{E}(z, t)] = \frac{1}{2}\tilde{E}_0(z, t)e^{i(kz - \omega t)} + \frac{1}{2}\tilde{E}_0^*(z, t)e^{-i(kz - \omega t)}. \quad (2.6)$$

We continue with the complex notation for the usual reason that manipulations, such as adding components of different phases, are much simpler.

By substituting (2.5) into (2.4) we obtain the simplest *dispersion relation* of $\omega = ck$, *i.e.* all frequencies travel at a speed c , a familiar result for light in vacuo. Such plane wave solutions will propagate without attenuation or dispersion, which is how we are able to look up at the night sky and observe light from distant stars that has travelled enormous distance through the void of interstellar space.

Light travelling through matter is a more complex problem. We next want to look for solutions to (2.4) in the presence of sources, such that we have $P \neq 0$ describing induced atomic dipoles in the medium. For that we will need to make a useful approximation.

2.2.2 The Slowly Varying Envelope Approximation

If the spectrum of the electric field is narrowband, we approximate the field as the product of a quasi-monochromatic *carrier* function with angular frequency ω and wavenumber k and a *slowly-varying envelope*

$$E(z, t) = \frac{1}{2}\mathcal{E}(z, t)e^{i(kz - \omega t)} + \frac{1}{2}\mathcal{E}^*(z, t)e^{-i(kz - \omega t)} \quad (2.7)$$

where the envelope is in general a complex function

$$\mathcal{E}(z, t) = |\mathcal{E}|e^{i\varphi}. \quad (2.8)$$

We apply the same treatment to the polarisation

$$P(z, t) = \frac{1}{2}\mathcal{P}(z, t)e^{i(kz - \omega t)} + \frac{1}{2}\mathcal{P}^*(z, t)e^{-i(kz - \omega t)} \quad (2.9)$$

with a polarisation envelope

$$\mathcal{P}(z, t) = |\mathcal{P}|e^{i\varphi}. \quad (2.10)$$

We can substitute these into (2.4) and by matching co-rotating terms we find

$$\left[(\partial_{zz} + 2ik\partial_z - k^2) - \frac{1}{c^2}(\partial_{tt} - 2i\omega\partial_t - \omega^2) \right] \mathcal{E} = \mu_0(\partial_{tt} - 2i\omega\partial_t - \omega^2)\mathcal{P}. \quad (2.11)$$

Now we're set to make the *slowly-varying envelope approximation*.⁴ If the envelope changes only a small amount over the distance of a wavelength, and over the duration of the optical period, we can take

$$\begin{aligned} |\partial_{zz}\mathcal{E}| &\ll k|\partial_z\mathcal{E}| \\ |\partial_{tt}\mathcal{E}| &\ll \omega|\partial_t\mathcal{E}| \end{aligned}$$

and neglect the second derivatives. Similar approximations hold for \mathcal{P} , where we may also neglect the first-order time derivative

$$\begin{aligned} |\partial_{zz}\mathcal{P}| &\ll k|\partial_z\mathcal{P}| \\ |\partial_{tt}\mathcal{E}| &\ll \omega|\partial_t\mathcal{E}| \\ |\partial_t\mathcal{P}| &\ll \omega|\mathcal{P}|. \end{aligned}$$

In the case of visible light with wavelengths on the order of 100 nm and optical periods of the order of 1 fs, where we're interested in the behaviour over ns or μ s, this approximation is justified.

With these approximations made, (2.11) becomes

$$\left[2ik\partial_z - k^2 + \frac{1}{c^2}(2i\omega\partial_t + \omega^2) \right] \mathcal{E} = -\mu_0\omega^2\mathcal{P} \quad (2.12)$$

As the carrier wavenumber and frequency are still related by the vacuum dispersion relation $\omega = ck$ we then obtain the first-order propagation equation

$$\left[\frac{\partial}{\partial z} + \frac{1}{c} \frac{\partial}{\partial t} \right] \mathcal{E} = i \frac{k}{2\epsilon_0} \mathcal{P}. \quad (2.13)$$

The wave equation (2.13), first-order in space z and time t , can be solved numerically for a given medium, to determine how light will propagate through it. But we will next need to determine how the media through \mathcal{P} is itself affected by the field \mathcal{E} .

2.2.3 Energy and Intensity

In an experiment we will not be measuring the electric field directly, but the energy transferred to a detector such as a photon counter. Also, any macroscopic measurement of light is necessarily going to extend over many optical cycles (of duration $\sim 10^{-15}$ s). So a property useful to us is the time-averaged power per unit area that the electromagnetic field transports through the medium, which we call the intensity I and is calculated to be⁵

$$I = \frac{1}{2}c\epsilon_0|\mathcal{E}^2|. \quad (2.14)$$

2.3 Linear Optics, Susceptibility and Refractive Index

The effect of an electric field \mathbf{E} applied on a single neutral atom is to separate the positively charged core (which moves in the direction of the field \mathbf{E}) and the negatively charged electron cloud (which moves in the opposite direction $-\mathbf{E}$) such that a dipole is induced on the atom parallel to the field. For an atomic vapour subject to a field, dipoles will be induced on many atoms. The cumulative effect is that the medium is polarised, and we define \mathbf{P} as the dipole moment per unit volume.

2.3.1 Susceptibility

In general, the instantaneous polarisation induced by the field at a time t is some function of the input field, which we may write as a power expansion² in \mathbf{E} ,

$$\mathbf{P}_{\text{inst}}(t) = \epsilon_0 \left[\chi^{(1)}(t)\mathbf{E}(t) + \chi^{(2)}(t)\mathbf{E}(t)^2 + \chi^{(3)}(t)\mathbf{E}(t)^3 + \dots \right] \quad (2.15)$$

where the expansion coefficients $\chi^{(j)}(t)$ are known as the j th- order susceptibilities.

If the applied field is weak, we find that the induced polarisation is proportional to that field, such that susceptibilities higher than $\chi^{(1)}$ are taken as zero and terms higher than the first order in (2.15) are neglected. This is the regime of *linear optics*. In this thesis we are particularly interested in developing and understanding numerical solutions of *nonlinear* problems, *i.e.* those in which higher order terms become significant. Systems involving weak fields are commonplace however, and as they permit analytic solution, along with offering insight into a broad range of optical phenomena, we will look at the linear regime briefly.

The cumulative induced polarisation $P(t)$ is an integral of the instantaneous polarisation over all times t' previous

$$P(t) = \varepsilon_0 \int_{-\infty}^t \chi(t') E(t - t') dt' \quad (2.16)$$

where we no longer require a superscript to define the linear susceptibility $\chi(t) := \chi^{(1)}(t)$. The upper limit on the integral expresses the causality condition that only the applied field at times in the past may affect the current state of the atoms.

So far we have described atomic response in the time domain, which is particularly useful when looking at time-dependent input fields such as short pulses. But it is also instructive to look at the frequency domain, which is advantageous when the input field is monochromatic. The change in perspective is effected as usual via the Fourier transform.³ We will use the convention for the transform on the electric field envelope $\mathcal{E}(t)$

$$\mathcal{E}(\omega) = \int_{-\infty}^{\infty} \mathcal{E}(t) e^{i\omega t} dt \quad (2.17)$$

and for the inverse

$$\mathcal{E}(t) = \frac{1}{2\pi} \int_{-\infty}^{\infty} \mathcal{E}(\omega) e^{-i\omega t} d\omega \quad (2.18)$$

and we define the transform in the same way for the polarisation envelope $\mathcal{P}(t)$.

Making the envelope and carrier ansatz as in (2.33) and substituting (2.18) into the right-hand side of (2.16), we get

$$\mathcal{P}(t) = \varepsilon_0 \int_{-\infty}^t \chi(t') \frac{1}{2\pi} \int_{-\infty}^{\infty} \mathcal{E}(\omega) e^{-i\omega(t-t')} d\omega dt'. \quad (2.19)$$

We now define the frequency-dependent linear susceptibility

$$\chi(\omega) := \int_{-\infty}^t \chi(t') e^{i\omega t'} dt' \quad (2.20)$$

such that

$$\mathcal{P}(t) = \frac{1}{2\pi} \int_{-\infty}^{\infty} \varepsilon_0 \chi(\omega) \mathcal{E}(\omega) e^{-i\omega t} d\omega. \quad (2.21)$$

This expression gives the time-dependent polarisation in terms of the frequency components of the field weighted by that frequency-dependent susceptibility function. We may then take the Fourier transform of the left-hand side and, as the equality holds for each frequency, we obtain the frequency domain linear response function

$$\mathcal{P}(\omega) = \varepsilon_0 \chi(\omega) \mathcal{E}(\omega). \quad (2.22)$$

We may now substitute this expression into (2.13), with $\mathcal{E}(\omega)$ time-independent by the definition (2.17), to obtain

$$\frac{\partial \mathcal{E}(z, \omega)}{\partial z} = i \frac{k}{2} \chi(\omega) \mathcal{E}(z, \omega). \quad (2.23)$$

This first-order differential equation in z has the analytical solution

$$\mathcal{E}(z, \omega) = e^{i \frac{k}{2} \chi z}. \quad (2.24)$$

Having determined an expression for the electric field envelope in terms of the frequency-dependent susceptibility, we can put this expression for the envelope into 2.13 in order to determine the effect it will have. It is useful to separate the real and imaginary parts of the susceptibility $\chi(\omega) := \chi_R(\omega) + i\chi_I(\omega)$, and we find

$$\mathcal{E}(z, \omega) = \mathcal{E}(0, \omega) e^{i(\frac{k}{2}\chi_R z)} e^{-\frac{k}{2}\chi_I z}. \quad (2.25)$$

The real part of the frequency dependent susceptibility then corresponds to a phase shift $\frac{k}{2}\chi_R z$ and so dispersion, and the imaginary part diminishes the field. As defined in (2.14) the intensity $I \propto |\mathcal{E}|^2$ and so is attenuated as it progresses through the medium via

$$I(z, \omega) = I_0(z, \omega)e^{-\alpha(\omega)z} \quad (2.26)$$

where the absorption coefficient $\alpha(\omega) := k\chi_I(\omega)$. This is the familiar Beer law of absorption for weak fields.

2.3.2 Refractive Index

If we return back to the Maxwell equations, we see by substitution of the susceptibility χ into the definition for dispersion (2.2), we get

$$\mathbf{D} = \epsilon_0(1 + \chi)\mathbf{E}. \quad (2.27)$$

Deriving the Maxwell wave equation again using this substitution, we find that the result is as for propagation in free space but with the vacuum speed c replaced with a general phase velocity

$$v_p = \frac{c}{\sqrt{1 + \chi}} = \frac{c}{n} \quad (2.28)$$

where n is the refractive index, familiar from geometrical optics. In most linear media χ is positive, so light travels more slowly in the medium.⁶

This leads us to consider what this velocity represents, considering that photons are massless and must travel at c .⁷ The resultant field wave is a superposition of the applied field wave and a secondary field wave which results from induced dipoles. In linear media, this resultant wave has the same carrier frequency but a different phase. The fact that the frequency is the same is the reason dense transparent materials exist. If the secondary wave lags the applied wave, the resultant wave will also lag. An observer in the medium will have to wait longer for the peaks

of the resultant wave to come past. It is this phase difference which leads to an apparently slower phase velocity. The refractive index represents the cumulative phase difference as the light moves through the medium.³

2.4 Interaction of Light with Atoms

We have seen in the weak field regime how the linear susceptibility relates to the absorptive and dispersive response of the medium. But we have not yet determined how that susceptibility relates to the properties of the atomic ensemble. Beyond the linear regime, the susceptibility is not a good descriptor for the response of the medium, and analytic expressions for the field propagation are not available. In the nonlinear regime, we will need to follow the dynamics of the atoms to determine how the field will propagate through the medium.

For the dynamics of atom-light interaction to be properly considered the system must be treated as an open quantum system. While the processes of absorption and stimulated emission (of photons from and to the applied field) can be described within a closed quantum system, the process of spontaneous decay due to interaction with vacuum fluctuations surrounding an atom cannot. As such, the time evolution is described by the Lindblad master equation

$$i\hbar \frac{\partial \rho}{\partial t} = [\mathcal{H}, \rho] + \mathcal{L} \{\rho\}. \quad (2.29)$$

The background of this equation and the conditions under which it is valid are discussed in appendix A. It constitutes a set of differential equations to be solved: one for each of the density matrix elements.

2.4.1 Spontaneous Decay of Excited States

As described in equation (A.9), coupling to the environment is implemented via the Lindblad superoperator \mathcal{L} which is completely defined by a finite set of collapse operators. In the case of spontaneous emission due to interaction with vacuum fluctuations, these are defined as

$$C_{ij} = \sqrt{\Gamma_{ij}} |i\rangle \langle j|. \quad (2.30)$$

where $\Gamma_{ij} = 1/\tau_{ij}$ and τ_{ij} is the stochastic rate at which electrons spontaneously decay from a higher state $|j\rangle$ to a lower state $|i\rangle$. The quantity Γ_{ij} is known as the natural linewidth for the specific transition $|i\rangle \rightarrow |j\rangle$, for reasons that will be clarified in section 2.5.

2.4.2 The Interaction Hamiltonian

A single-electron (or hydrogenic) atom has a positively charged nucleus and a negatively charged electron, both of which will interact with an applied electromagnetic field. At optical wavelengths, however, the interaction with the nucleus is negligible,⁸ so we focus our attention on the electron.

Without interaction with an external field, the bare atomic Hamiltonian is given by

$$\mathcal{H}_0 = \frac{\mathbf{p}^2}{2m_e} + V(r) \quad (2.31)$$

where m_e is the mass of the electron, \mathbf{r} and $\mathbf{p} = i\hbar\nabla$ are its position and momentum operators, and $V(r)$ is the spherical atomic potential.

The non-relativistic Hamiltonian of the electron interacting with an applied classical electric field \mathbf{E} , in the Coulomb gauge, may be written

$$\mathcal{H} = \mathcal{H}_0 + \mathcal{H}_I \quad (2.32)$$

where the interaction Hamiltonian term \mathcal{H}_I describes the coupling of the atomic dipole to the field.⁸ The problem of the atom-light interaction is then one of calculating the matrix elements of \mathcal{H}_I as a perturbation to the eigenstate basis of \mathcal{H}_0 .

We will consider a monochromatic field with angular frequency ω and wavenumber \mathbf{k} (the analysis extends to multi-chromatic fields, which we will consider in chapter 3). We may write the field as

$$\mathbf{E}(\mathbf{r}, t) = \hat{\mathbf{x}} \left[\frac{1}{2} \mathcal{E}(t) e^{i(\mathbf{k} \cdot \mathbf{r} - \omega t)} + \frac{1}{2} \mathcal{E}^*(t) e^{-i(\mathbf{k} \cdot \mathbf{r} - \omega t)} \right] \quad (2.33)$$

where $\hat{\mathbf{x}}$ is the unit polarisation vector and $\mathcal{E}(t)$ is the field amplitude.

We simplify calculation of matrix elements by making the exponential expansion

$$e^{i\mathbf{k} \cdot \mathbf{r}} \approx 1 + (i\mathbf{k} \cdot \mathbf{r}) + \frac{1}{2!} (i\mathbf{k} \cdot \mathbf{r})^2 + \dots \quad (2.34)$$

and neglecting all but the first term, unity. This *electric dipole approximation*⁹ represents neglecting the spatial dependence of the field over the extent of the atom, and is justified as the electronic wavefunction is on the order of the Bohr radius at 10^{-10} m and the optical carrier wavelength $\lambda = 2\pi/k$ is on the order of 10^{-7} m. The approximation may equivalently be derived as truncating a multipole expansion of the interaction at the dipole term.¹⁰

Applying the electric dipole approximation, we may write the interaction Hamiltonian term as

$$\mathcal{H}_I = -e\mathbf{r} \cdot \mathbf{E} = -\mathbf{d} \cdot \mathbf{E} \quad (2.35)$$

where analogous with a classical dipole moment, \mathbf{d} is the electric dipole operator. And we may take the field out of the spatial integral implicit in calculating the matrix elements between two bare atom eigenstates $|a\rangle$

and $|b\rangle$,

$$\begin{aligned}\langle a | \mathcal{H}_I | b \rangle &= - \left[\frac{1}{2} \mathcal{E}(t) e^{-i\omega t} + \frac{1}{2} \mathcal{E}^*(t) e^{i\omega t} \right] \langle a | \hat{\mathbf{x}} \cdot e\mathbf{r} | b \rangle \\ &= - \left[\frac{1}{2} \mathcal{E}(t) e^{-i\omega t} + \frac{1}{2} \mathcal{E}^*(t) e^{i\omega t} \right] d_{ab}\end{aligned}\quad (2.36)$$

where d_{ab} is then the matrix element of the electric dipole operator \mathbf{d} projected on the polarisation direction of the electric field. The crux of the problem is then in calculating (or looking up) dipole matrix elements for the eigenstates of a given system.

2.4.3 Dipole Matrix Elements and Parity

We can show that the diagonal matrix elements of $\mathbf{d} = e\mathbf{r}$ are zero by making a parity argument. We define the parity operator Π as the unitary operator (i.e. $\Pi^\dagger \Pi = 1$) that flips the sign of the position operator \mathbf{r} via

$$\Pi \mathbf{r} \Pi^\dagger = -\mathbf{r}. \quad (2.37)$$

Operating with Π on the right of both sides shows that the anticommutator $\{\Pi, \mathbf{r}\} = \Pi \mathbf{r} + \mathbf{r} \Pi = 0$ and thus the matrix elements vanish

$$\langle i | \{\Pi, \mathbf{r}\} | j \rangle = \langle i | \Pi \mathbf{r} + \mathbf{r} \Pi | j \rangle = 0 \quad (2.38)$$

for any states $|i\rangle, |j\rangle$. Now Π commutes with \mathcal{H} , and so has the same eigenstates, so we have eigenvalues π_i, π_j such that $\Pi |i\rangle = \pi_i |i\rangle$ and $\Pi |j\rangle = \pi_j |j\rangle$. Thus we can write

$$\langle i | \Pi \mathbf{r} + \mathbf{r} \Pi | j \rangle = (\pi_i + \pi_j) \langle i | \mathbf{r} | j \rangle. \quad (2.39)$$

The right hand side can only be zero if $\pi_i + \pi_j$ is zero or if the matrix element is. Now, as $\Pi^2 = 1$, the eigenvalues $\pi = \pm 1$. So for the diagonal matrix elements, $\pi_i + \pi_i$ can't be zero and $\pi_j + \pi_j$ can't be zero so it must be that $\langle i | \mathbf{r} | i \rangle = \langle j | \mathbf{r} | j \rangle = 0$. The off-diagonal matrix elements $\langle i | \mathbf{r} | j \rangle$ are non-vanishing if the states have opposite parity such that $\pi_i = -\pi_j$.

2.4.4 Atomic Coherence and Polarisation

We introduced the polarisation P in section 2.2 as the cumulative effect of charge separation induced on individual atoms and defined it in 2.3 as the dipole moment per unit volume. In terms of atomic observables, the polarisation at a distance z through the medium at time t may therefore be written as the expectation value of the scalar dipole operator for those atoms

$$P(z, t) = N(z) \langle d(z, t) \rangle \quad (2.40)$$

where $N(z)$ is the number density (atoms per unit volume) of the medium, which may in general be a function of propagation distance z , for example in an atom cloud shaped by the geometry of a magneto-optical trap,¹¹ or constant for a thermal cell in thermal equilibrium.

The expectation value of an observable for a system in a pure or mixed state represented by a density matrix ρ is defined in equation (A.5), such that we may write

$$P(z, t) = N(z) \text{Tr} [\rho d(z, t)]. \quad (2.41)$$

As we know from the above parity argument that the diagonal matrix elements of the dipole operator are zero, we may then write P directly in terms of the off-diagonal elements and the atomic coherences, via

$$P(z, t) = N(z) \sum_{i \neq j} [d_{ij}\rho_{ij}(z, t) + d_{ji}\rho_{ji}(z, t)]. \quad (2.42)$$

Now in order to relate this to the slowly-varying envelope \mathcal{P} , we need to rotate the density matrix elements, via

$$\begin{aligned} \rho_{ij} &= \tilde{\rho}_{ij} e^{i(kz - \omega t)} \\ \rho_{ji} &= \rho_{ij}^* = \tilde{\rho}_{ij}^* e^{-i(kz - \omega t)} \end{aligned}$$

where tilde-notated variables $\tilde{\rho}_{ij}$ are slowly-varying density matrix elements. Dropping the tilde notation, we then derive an expression for the

slowly-varying polarisation envelope in terms of the atomic coherences

$$\mathcal{P}(z, t) = N(z) \sum_{i \neq j} d_{ij} \rho_{ij}(z, t) \quad (2.43)$$

which we may substitute into the propagation equation (2.13).

Note that in our discussion of polarisation in this section we have made no reference to the susceptibilities $\chi^{(j)}(t)$. These are implicit in the density matrix coherences. This analysis is valid for any general nonlinear form of polarisation as expressed in equation (2.15) if we can determine the evolution of atomic states from the Lindblad equation (2.29).

2.4.5 Thermal Atoms

The above analysis for the atom-light interaction is appropriate for stationary (*i.e.* ultracold) atoms but must be modified for thermal atoms due to the averaging effect of atomic motion.¹²

An atom moving with a velocity component v in the z -direction will interact with a Doppler-shifted field frequency $\omega - kv$. This shift is effected over a 1D Maxwell-Boltzmann probability distribution function of velocity^{13, 14}

$$f(v) = \frac{1}{u\sqrt{\pi}} e^{-(kv/u)^2} \quad (2.44)$$

where the thermal width $u = kv_w$. Here k is again the wavenumber of the quasi-monochromatic field and $v_w = 2k_B T / m$ is the most probable speed of the Maxwell-Boltzmann distribution for a temperature T and atomic mass m . As is usual, k_B represents the Boltzmann constant.

To include this Doppler effect in the field propagation equations (2.13), we replace the atomic coherence factor by an integral over a convolution of $f(v)$, with the atomic coherence now a function of velocity, so that

$$\mathcal{P}(z, t) = N \sum_{i \neq j} d_{ij} \int_{-\infty}^{\infty} \rho_{ij}(z, t; v) f(v) dv. \quad (2.45)$$

This velocity-dependent $\rho_{ij}(z, t; v)$ represents the atomic coherence resulting from interaction with a field at the Doppler-shifted frequency $\omega - kv$.

The result of the inclusion of thermal effects is a broadening of absorption resonance widths, a familiar concern in spectroscopy. We will consider example spectral profiles in section 2.5.

2.4.6 Shifting to the Speed-of-Light Reference Frame

To solve the propagation equation (2.13) as a boundary value problem, it is useful to introduce co-moving variables $\zeta = z$ and $t' = t - z/c$. This is equivalent to using a reference frame that moves with the speed of light across the medium.¹² We then have

$$\frac{\partial}{\partial \zeta} = \frac{\partial z}{\partial \zeta} \frac{\partial}{\partial z} + \frac{\partial t}{\partial \zeta} \frac{\partial}{\partial t} = \frac{\partial}{\partial z} + \frac{1}{c} \frac{\partial}{\partial t} \quad (2.46)$$

so that

$$\frac{\partial}{\partial z} \mathcal{E}(z, t') = i \frac{k}{2\epsilon_0} N(z) \sum_{i \neq j} d_{ij} \int_{-\infty}^{\infty} \rho_{ij}(z, t; v) f(v) dv. \quad (2.47)$$

In this reference frame we see that the propagation equation for the field is now a differential equation only in z .

2.4.7 A Recap

At this point we have derived a set of coupled partial differential equations describing the dynamics of the atomic density operator (2.29) and the propagation of the electric field envelope (2.47).

These coupled equations can be integrated numerically for a given set of boundary conditions defining the input profile of the electric field and the initial state of the atoms. The integration proceeds via the following recipe, which must be repeated in a self-consistent manner:

1. Solve the Lindblad master equation for the quantal dynamics of the atomic density matrix over time t' .
2. Average the Maxwell-Boltzmann probability distribution over velocity v .
3. Solve the Maxwell wave equations for propagation of the electro-magnetic field over space z .

The description of the specific numerical algorithms used for integration, along with details of the Python code used to implement these algorithms, is given in appendices B and C. We will make use of these methods to solve the MB equations for various systems of interest throughout the chapters of this thesis.

2.5 Linear Propagation in Two-level Atoms

Now that we have derived the necessary differential equations to describe 1D propagation in an atomic vapour and described computational algorithms for the numerical solution of the problem for a given set of boundary conditions, we will look at example results from simulated propagation of a monochromatic (*i.e.* single carrier frequency) field in a simple two-level system.

We will define the two-level system and present the results of propagation for some boundary conditions representative of laboratory experiments: pulsed and continuous-wave (cw) input fields. We'll then make an analysis of the frequency dependent behaviour of the simulated propagation of a wider-spectrum field. We will use these results to verify that these results match the known analytic response functions for the linear regime, such that we have confidence in the computational

scheme for the simulations we will later obtain for nonlinear systems with more than one carrier frequency.

We will also introduce the natural unit system which will be used throughout this thesis.

2.5.1 The Two-level System

No real atomic system exists with only two levels of course, but this minimal scheme is a good approximation in the case of resonant interaction with a well-separated transition.

The system is defined by a Hilbert space covered by a basis that consists of a ground state $|0\rangle$ and an excited state $|1\rangle$ with eigenenergies E_0 and E_1 . The resonance frequency $\omega_0 = (E_1 - E_0)/\hbar$. As is conventional we define the detuning of the input carrier frequency from resonance as $\Delta = \omega - \omega_0$ and the complex Rabi frequency¹⁵

$$\Omega(z, t) = \frac{d_{01}}{\hbar} \mathcal{E}(z, t) \quad (2.48)$$

where $d_{01} = \langle 0 | d | 1 \rangle$ is the transition dipole matrix element.

The time evolution is independent of the absolute value of the bare state energies, so we may set the ground state energy $E_0 = 0$. Making the rotating wave approximation, we find that the atomic Hamiltonian is given by

$$\mathcal{H} = \hbar \begin{bmatrix} 0 & \Omega/2 \\ \Omega^*/2 & -\Delta \end{bmatrix} \quad (2.49)$$

in the frame rotating with the carrier frequency.¹⁶

For the Lindblad superoperator \mathcal{L} we have just a single collapse operator representing spontaneous decay of the electron from the the excited state to the ground state

$$C = \sqrt{\Gamma} |0\rangle\langle 1|. \quad (2.50)$$

In two-level medium we only have one dipole matrix element and one coherence to consider, such that (neglecting the Doppler effect for now) the propagation equation (2.47) may be written

$$\frac{\partial}{\partial z} \mathcal{E}(z, t') = iN(z) \frac{k}{2\epsilon_0} d_{01} \cdot \rho_{01}(z, t'). \quad (2.51)$$

It is useful to write the propagation now in terms of the Rabi frequency

$$\frac{\partial}{\partial z} \Omega(z, t') = iN(z) g \cdot \rho_{01}(z, t') \quad (2.52)$$

where we define a propagation coefficient

$$g_{01} = \frac{d_{01}^2 k}{2\epsilon_0 \hbar} \quad (2.53)$$

which is constant for a given transition with dipole matrix element d_{01} and for a field with carrier wavenumber k .

2.5.2 The Natural Unit System

For a two-level system we have a single natural linewidth, and so it is convenient to introduce a natural unit system, with frequencies in units of the natural linewidth Γ , times in terms of the reciprocal spontaneous decay lifetime $\tau = 1/\Gamma$ and distances in terms of the length of the medium L .

To give an illustrative example, we will take a rubidium 85 cell and apply a monochromatic field on resonance with the D1 transition from the $5^2S_{1/2}$ ground state to the $5^2P_{1/2}$ excited state at $\omega = 2\pi \times 377$ THz. The spontaneous decay rate for the transition $\Gamma = 2\pi \times 5.75$ MHz such that the lifetime $\tau = 27.6$ ns. The transition dipole matrix element is $d_{01} = 2.53 \cdot 10^{-29}$ C m. From this we can calculate that the propagation coefficient for the transition $g_{01} = 2\pi \times 4.34 \cdot 10^{-9}$ MHz cm².

The number density N in a contained cell is a function of the temperature of the cell. For an example temperature $T = 200$ C we have $N =$

$9.26 \cdot 10^{14} \text{ cm}^{-3}$. If we then take a cell of a typical length $L = 1 \text{ mm}$, the key parameter we require for describing propagation in the medium can be expressed purely in terms of the natural units as $N g_{01} = 2\pi \times 70 \Gamma / L$.

By introducing this natural unit system we are able to reduce the number of parameters involved in the mathematical problem. For example, it becomes clear that increasing the length of the medium ten times is equivalent to raising the number density by the same scale, or by choosing a system with a suitably higher dipole moment.

2.5.3 Weak Probe Lineshape

The Lindblad master equation (2.29) represents a set of differential equations in time for the time evolution of each density matrix element.

As we know via equation (2.43) that the polarisation \mathcal{P} is related to the off-diagonal coherence ρ_{01} , we write out the particular equation to follow its time evolution, such that

$$\frac{d\rho}{dt} = i\Omega(\rho_{00} - \rho_{11}) + \left(i\Delta - \frac{\Gamma}{2}\right)\rho_{10}. \quad (2.54)$$

In the case of weak field input on the medium, we may assume that we're in a quasi-static regime where the atomic density matrix changes negligibly over the time of the input. We thus set the time derivative in equation (2.54) to zero.

The initial condition is that all of the atomic population starts in the ground state. For a weak field we may also assume that population transfer is negligible such that $\rho_{11} = 0$.

Under these weak field approximations, we may thus derive the steady state, weak field lineshape

$$\rho_{01}(z) = -\Omega(z) \frac{1}{i\frac{\Gamma}{2} + \Delta}. \quad (2.55)$$

2.5.4 Weak Pulse Propagation Results

The first Maxwell-Bloch simulation results we will consider are for an input field profile of finite duration, namely a Gaussian pulse. In general for short duration pulses, the atoms do not reach equilibrium with the applied field before the pulse has passed, however for weak fields so little population is transferred that a quasi-static regime can be a good approximation.

The Gaussian pulsed input field is defined by

$$\Omega(t) = \Omega_0 \exp \left[-4 \log 2 \left(\frac{t - t_0}{t_w} \right) \right] \quad (2.56)$$

where Ω_0 is the peak input Rabi frequency, t_0 is the time at which the function reaches that peak, and t_w is the full width at half maximum (FWHM) of the pulse.

In this simulation we let the peak $\Omega_0 = 2\pi \times 10^{-3} \Gamma$, the centre $t_0 = 0$ and the width $t_w = 0.1 \tau$. We define the medium to have a length L , number density N and coupling g such that the key absorption parameter $Ng = 2\pi \times 1 \Gamma/L$.

In figure 2.1 we present a colour map of the simulated real part of the complex Rabi frequency $\Omega(z, t)$ describing the field profile as it propagates through the medium.

Time t is shown on the x -axis and the propagation distance z is shown on the y -axis such that the field enters at the bottom of the plot. The horizontal slice at $z = 0$ thus represents the Gaussian input field. All propagation results are presented in the speed-of-light reference frame described in section 2.4.

We see that the primary pulse envelope is attenuated and slightly fast, such that the first peak arrives at the rear of the medium, $z = 1L$, at a time $t \approx -0.05 \tau$ in the speed-of-light reference frame. [normal disper-

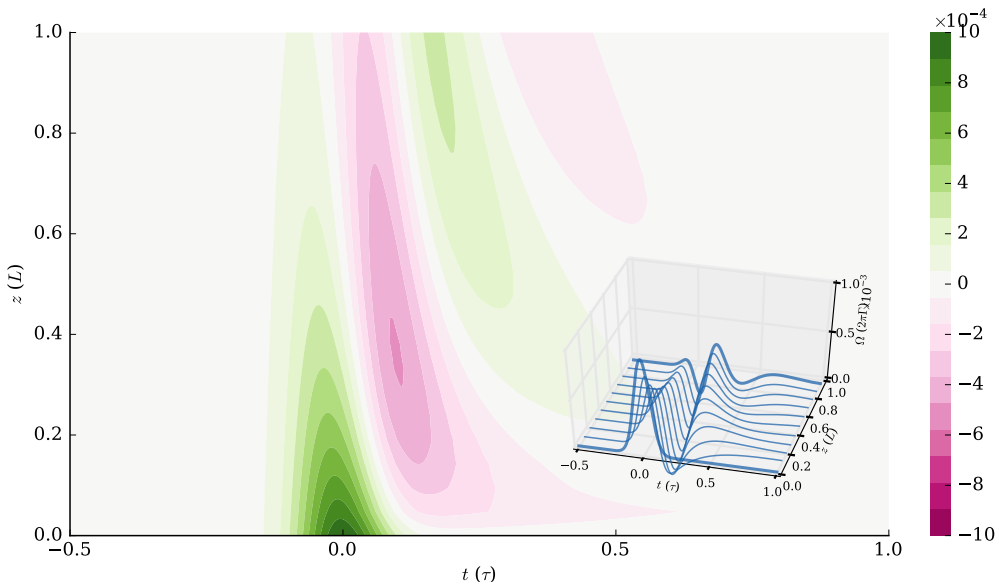


FIGURE 2.1 The real part of the complex Rabi frequency $\Omega(z, t)$ showing the simulated result of propagation of a weak pulse through a two-level medium. (Inset 3D) The field has Gaussian profile entering the medium at $z = 0$, with peak $\Omega_0 = 2\pi \times 10^{-3} \Gamma$ and width $t_w = 0.1 \tau$.

sion profile]. Not all of the energy of the pulse is absorbed, however. This is because the pulse is short in duration relative to τ , such that its spectral profile is wider in frequency space than the absorption window of the atoms. Thus some spectral components of the field see a medium which is transparent to them. However, they remain subject to phase shift. We see high-frequency ringing, also described as a 0π pulse as the total area integrates to zero.^{16, 17}

In figure 2.2 we present colour maps of simulated density matrix elements describing the response of the atoms along the medium as the applied field reaches them.

The cumulative Rabi frequency of the pulse is many orders of magnitude too small to saturate the excited state population so that for the atoms at the front of the medium at $z = 0$, ρ_{11} continues to rise through the pulse to a peak at time $t \approx 0.01 \tau$ after the input field has peaked. There is a small ‘echo’ in the excited state, due to the field ringing, visi-

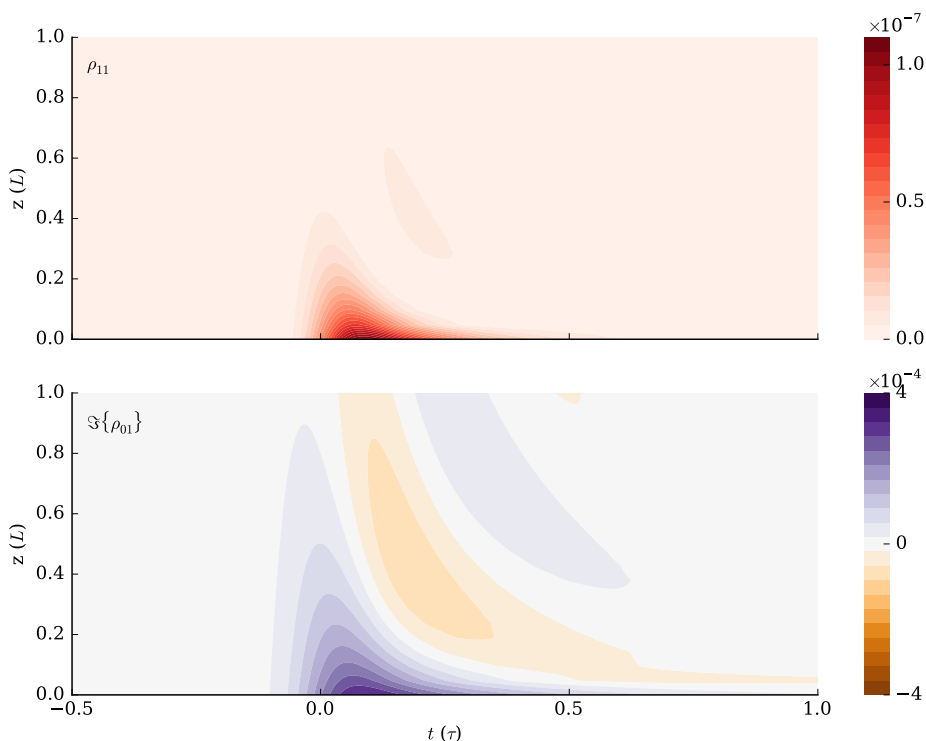


FIGURE 2.2 Density matrix elements of the two-level atom system as a function of z and t during the simulation. (Top) Excited state population $\rho_{11}(z, t)$. (Bottom) Coherence $\rho_{01}(z, t)$ between the states. The simulation parameters and boundary conditions are as for figure 2.1.

ble at $t \approx 0.2\tau$ and between $z = 0.4L$ and $0.6L$.

A positive imaginary coherence $\Im[\rho_{01}]$ is driven by the applied field at the front of the medium. We observe that the coherence decays at half the rate of the excited state population, $\Gamma/2$, consistent with equation (2.54).

2.5.5 Spectral Analysis

In section 2.3 we made use of Fourier transforms to shift perspective to the frequency domain. We showed that in the linear regime it is possible to derive a response function, given in equation (2.22), which when substituted into the propagation equation allows us to understand how the susceptibility describes the frequency-dependent absorptive and dispersive properties of a medium with respect to a weak field.

In order to verify the numerical model we have developed, as well as to demonstrate these spectral properties, we will now look at results from a simulation of a pulse propagating through the two-level medium. We wish to confirm that the results of the simulation match the known analytic response functions for the linear regime.

For this simulation we define an unusual and artificial time profile for the input field boundary condition: a cardinal sine (sinc) function given by

$$\Omega(t) = \frac{1}{20\sqrt{2\pi}} \text{sinc}(10t). \quad (2.57)$$

This input profile, shown in the top subplot of figure 2.3, is clearly impractical for any experimental setup. We choose this profile because its Fourier transform, shown in the bottom subplot of figure 2.3, is a square function with a width of 10Γ . This gives us a wide spectral range over which to observe the effect of the two-level medium on the field.

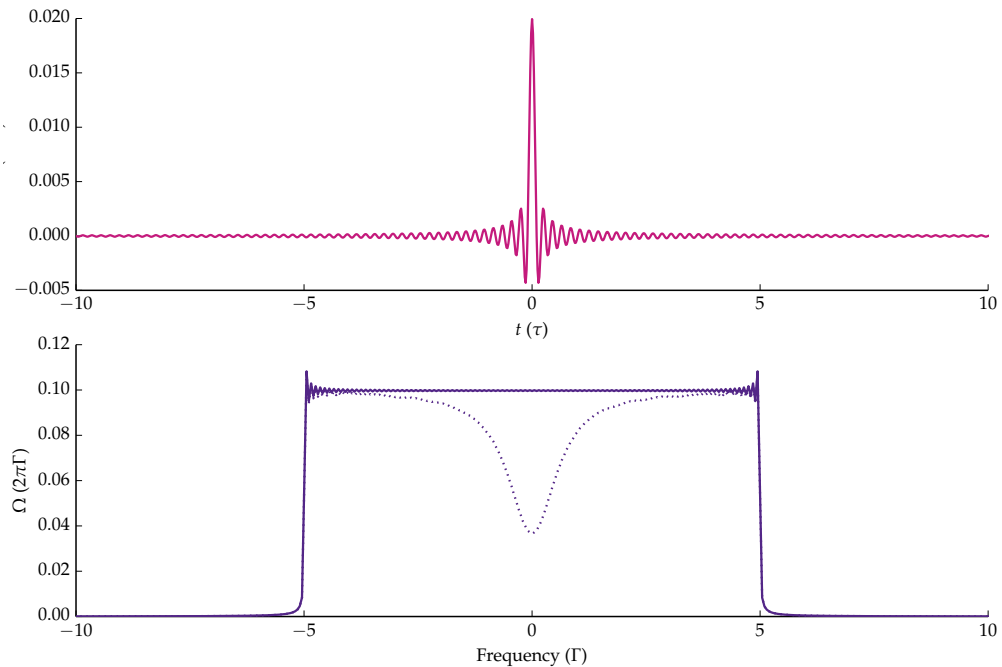


FIGURE 2.3 (Top) The sinc function (pink) defined by equation (2.57) which forms a simulated pulse profile in time $\Omega(t, 0)$ entering the medium at $z = 0$, *i.e.* the boundary condition. (Bottom) (Purple solid) The discrete Fourier transform $|\Omega(\omega, 0)|$ of the sinc shape above, representing the same function in the frequency domain at $z = 0$. (Purple dotted) The resulting field profile $|\Omega(\omega, z = 1)|$ in the frequency domain at $z = 1 L$, after propagation through the medium. The medium is defined with a length L , number density N and coupling g such that $Ng = 2\pi 1 \Gamma / L$.

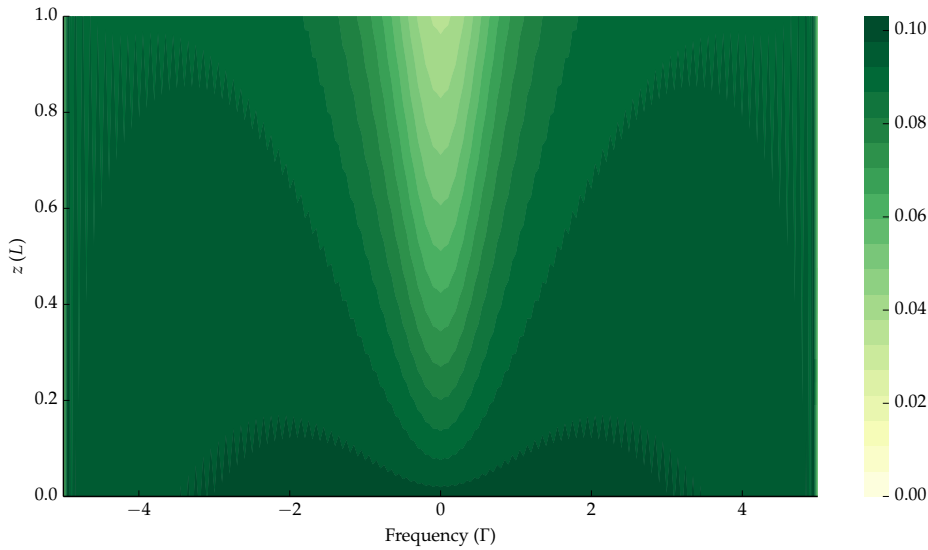


FIGURE 2.4 Magnitude of the Fourier-transformed Rabi frequency $|\Omega(z, \omega)|$, showing propagation of the field through the medium in the frequency domain during the simulation. The input boundary condition field profile at $z = 0$ is the sinc function shown in figure 2.3. The medium is defined with a length L and number density N such that $Ng = 2\pi 1\Gamma/L$.

The discrete Fourier transform (DFT) is used as the numerical method for shifting to the frequency domain, which results in some Gibbs ringing¹⁸ seen at the corners at $\pm 5\Gamma$.

A more-realistic Gaussian time profile, short in duration, would also cover a wide spectral range. We choose the sinc function for the reason that it provides greater accuracy in the wings far away from resonance, where both the input and output field amplitudes would be extremely small for the Gaussian function, bringing inaccuracy as we get close to limits for floating point storage.

The absorptive effect of the medium is immediately visible if we compare the $|\Omega(\omega, z=1)|$, the profile at the back of the medium, also shown (dotted) in the bottom subplot of figure 2.3. Around resonance there is a significant dip of around 60% in the transmitted Rabi frequency (and thus the electric field amplitude).

In figure 2.4 we show the results for $|\Omega(\omega, z)|$ as the sinc pulse moves through the medium. On resonance, the field decays exponentially while in the spectral wings we see nearly full transmission.

We can compare the simulated result with the analytic expression given in equation (2.25), which tells us that we can obtain the imaginary part of the susceptibility by checking the attenuation of the field via

$$\frac{k}{2}\chi_I(\omega)z = -\log \frac{|\Omega(z, \omega)|}{|\Omega(z = 0, \omega)|} \quad (2.58)$$

and the real part of the susceptibility by checking the phase shift over the medium,

$$\frac{k}{2}\chi_I(\omega)z = \phi(z, \omega) - \phi(z = 0, \omega) \quad (2.59)$$

where the ϕ is defined via

$$\Omega(z, \omega) = |\Omega|e^{i\phi}. \quad (2.60)$$

In figure 2.5 we present the simulated results for the susceptibility as defined in (2.58) and (2.59).

We see that the imaginary part, describing absorption of the field, has the Lorentzian lineshape familiar as a solution for classical systems involving forced and damped resonance. The FWHM is measured numerically, and as we would expect it is equal to 1Γ , the natural linewidth around which we designed the natural unit system.

Absorption linewidths observed in experiment will in general be significantly wider, as the important effects of Doppler broadening and atomic collisions must be considered. This natural linewidth represents the theoretical minimum linewidth that could be observed for cold atoms due to spontaneous emission rate, which for an atom in free space can never be reduced.¹⁵

The real component has the familiar dispersion lineshape describing the

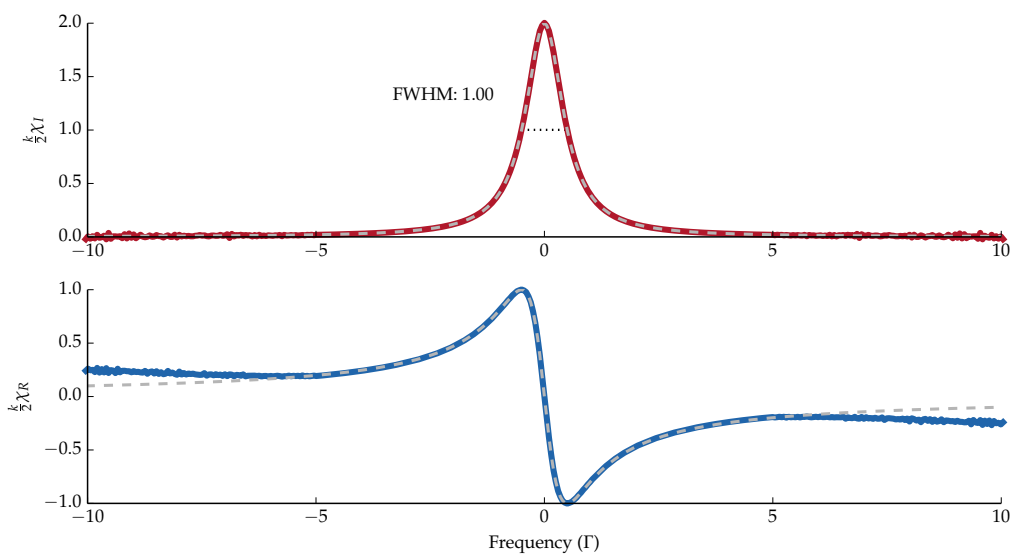


FIGURE 2.5 (Top) (red solid) The imaginary part of the linear susceptibility χ_I derived from the simulation via equation (2.58). (Bottom) (blue solid) The real part of the linear susceptibility χ_R derived from the simulation via equation (2.59). (grey dashed) Analytic functions of χ_I and χ_R derived from the weak probe lineshape given in equation (2.61). The FWHM of the χ_I lineshape is shown as measured numerically.

phase of the input field relative to the frequency of the oscillator as it passes over resonance from lagging to leading.³

By comparing the linear propagation equation (2.23) with the weak probe approximation for the coherence, given in equation (2.55), we note that we can also derive an analytic expression for the frequency-dependent susceptibility in this regime,

$$\frac{k}{2}\chi(\omega) = -Ng\frac{1}{i\frac{\Gamma}{2} + \Delta}. \quad (2.61)$$

The real and imaginary parts of this function are overlaid (grey dashed lines) on the simulated results and we see excellent agreement around resonance. We see in (2.61) that the imaginary part of the susceptibility, and thus the absorption, is solely due to the spontaneous decay term Γ . This we can understand as it is this scattering of energy by the atoms to the environment which results in a loss of energy in the system.

Spectral field components beyond $\pm 5\Gamma$ are negligible (as defined by the sinc function, see figure 2.3) and so we see some noise in the result beyond this point. We also see deviation between the analytic and simulated results in the dispersion profile far from resonance, which is due to the linear susceptibility approximation being valid only for near-resonant components of the field.

This result tells us that the computational scheme designed to model propagation of light in atomic media is accurate in the linear regime, which gives us confidence in the scheme for the work we will do later going beyond this weak field limit.

In the scope of input field boundary conditions, at the other extreme to short duration, wide-spectral pulses are continuous wave (cw) fields, with constant intensity over time. Such field envelopes are monochromatic, meaning that the frequency domain representation of a cw field in the time domain is a Dirac delta function.

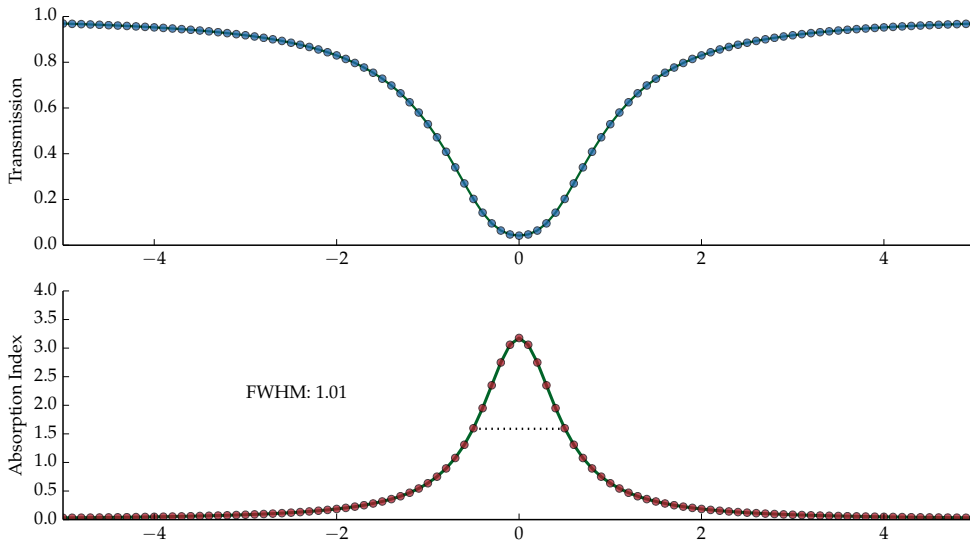


FIGURE 2.6 Peak transmission (top) and absorptive index (bottom) for a monochromatic cw field across a discrete range of 100 detunings Δ around resonance. The solid lines in both represent the same values for the continuous spectrum deriving from propagation of the short sinc pulse function.

In figure 2.6 we make a scan of the field detuning Δ across resonance with the two-level atom, and mark the peak transmission ($T = I/I_0$) of the field along with the associated absorptive index.

We also plot the transmission and absorption index of the transmission and absorption as a function of frequency for the wide-spectrum sinc pulse. The close agreement tells us that the short pulse's propagation is as if it were composed of many monochromatic frequency components interacting independently with the medium. In the linear regime, the solution is a superposition of individual frequencies.²

2.5.6 The Voigt Profile

As mentioned, the lineshapes presented thus far for weak probe spectra neglect the thermal motion of the atoms, and so are only valid for atoms that are stationary, *i.e.* close to absolute zero.

To account for thermal atoms, we must include the Doppler effect by means of the average over detunings described by the integral in equation 2.45. The thermal lineshape function may then be expressed as

$$s(\Delta) = \int_{-\infty}^{\infty} h(\Delta - kv) \times f(v) dv \quad (2.62)$$

where the weak probe natural lineshape

$$h(\Delta) = -Ng \frac{1}{i\frac{\Gamma}{2} + \Delta} \quad (2.63)$$

is given in equation (2.61) and $f(v)$ is the Maxwell- Boltzmann distribution over atomic velocities v given in equation (6.4).

Using the convolution theorem for Fourier transforms, this integral can be computed as

$$s(\Delta) = \frac{i\sqrt{\pi}}{2u} e^{-z^2} \times \text{erfc}(-iz) \quad (2.64)$$

where $z = ia/2 + b$ given $a = \Gamma/u$ and $b = \Delta/u$, and erfc is the complementary error function.¹⁹ This convolution of a Lorentzian function with a Gaussian function is known as a Voigt profile.

In figure we show simulated results for the real and imaginary parts of the susceptibility for the same system as in figure 2.5, but this time including Doppler effects in the numerical algorithm by a weighted averaging over a range of velocity classes as described in appendix C. We take the thermal width to be $u = 2\pi \times 0.5 \Gamma$. As an example, this might correspond to a ~ 0.1 mK vapour of ^{85}Rb probed on the D1 line.

We compare these simulated lineshapes with the weak probe Voigt profile given in equation (2.64) and see agreement with the analytic result. We see that the inclusion of temperature in the model has the effect of broadening the spectral lineshapes.

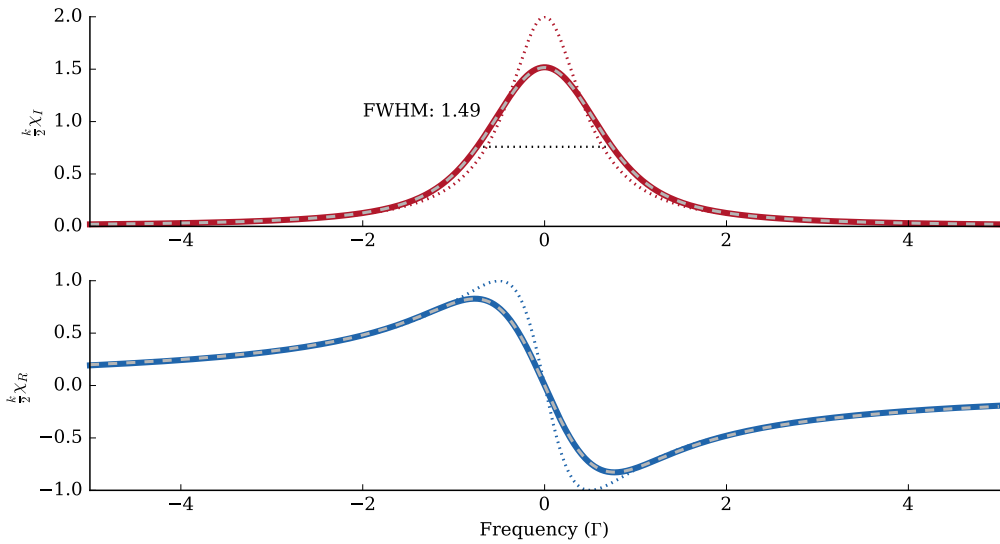


FIGURE 2.7 Top) The imaginary part of the linear susceptibility χ_I derived from a thermal simulation via equation (2.58). (Bottom) (blue solid) The real part of the linear susceptibility χ_R derived via equation (2.59). (grey dashed) Analytic functions of χ_I and χ_R derived from the convoluted Voigt profile given in equation (2.64).

2.6 Discussion

In this chapter we started from the Maxwell equations and derived a propagation equation for monochromatic light, using the slowly varying envelope approximation. We introduced the linear and nonlinear optics, and for the linear regime, for weak fields, the useful concept of susceptibility and how this relates to the absorptive and dispersive response of the medium.

Going beyond the linear regime, we need to follow the quantal dynamics of the atomic density matrix, which we do with the Lindblad master equation. We defined the interaction Hamiltonian within the electric dipole approximation, and how the polarisation of the medium can be derived from atomic coherences. For thermal atoms this coherence must be averaged over a Maxwell-Boltzmann distribution. We discussed algo-

rithms (presented in appendix C) for integrating the propagation equations numerically for nonlinear propagation.

We presented results for a two-level system in the linear regime. In doing so we used spectral analysis to compare with the analytic results derived in this regime. The good agreement in these results gives us confidence in the numerical methods. In the next chapter, we will employ the model in considering nonlinear pulse propagation in two-level and three-level systems.

3 Nonlinear Propagation Phenomena

4 Storage and Retrieval of Dark-State Polaritons

5 Two-Photon Excitation in a High-Intensity Beam

6 Propagation of Short Pulses in V-type Atoms

6.1 Introduction

In previous chapters we have investigated a subset of the fascinating array of phenomena that have been studied in the propagation of resonant optical beams in three-level media. We looked at the extension of the well-known effect of SIT and optical solitons to multtons in V-type media in chapter 3, and the propagation of dark-state polaritons under EIT conditions in Λ -type media in chapter 4.

In this chapter we return our attention to the propagation of light through atoms in the V-type system. Our motivation for this theoretical investigation is recent experimental work at Durham into coherent atomic dynamics on the sub-nanosecond timescale in thin (on the order of a micron in length) vapour cells.²⁰ The experiment is designed to investigate the effect on susceptibility of a medium with respect to a probe beam when significant population has been transferred into an excited state via a second, strong pulse.

If the two pulses were of the same wavelength, addressing the same transition, it would be experimentally difficult to separate detection of the probe signal in order to determine how its propagation had

been affected. In addition, the decay time of the excited state (on the order of nanoseconds) is too short for the pulses to be well-separated in time while maintaining the required population transfer in the medium. Thus, a second laser on a separate wavelength is used for the coupling field.

Similar systems have been designed to transfer population on the order of nanoseconds in rubidium vapours, using the Ξ (ladder) scheme to couple an excited state to a higher Rydberg state.^{21,22} However, the optical power required is prohibitively large due to the weak transition strength, so the experiment makes use again of the V-type configuration, coupling the ground state of rubidium to a pair of non-degenerate excited states.

In the next section we shall briefly describe the experiment and present results, before we go on to describe the theoretical model.

6.2 Description of the Experiment

A dense thermal vapour of rubidium atoms in their natural isotopic abundances, contained in a thin cell on the order of a micron in length, is addressed with two co-propagating monochromatic lasers, forming the V-type excitation scheme illustrated in figure 6.1(a). The probe laser is resonant with the D1 transition from the $5^2S_{1/2}$ ground state to the $5^2P_{1/2}$ excited state and the coupling laser is resonant with the D2 transition coupling the ground state to the $5^2P_{3/2}$ excited state.^{23,24} The beams are linearly polarised and orthogonal, and following propagation they are separated by a polarising beam splitter.

The $5^2S_{1/2}$ ground state in rubidium is a doublet state split on the order of GHz,²⁵ as shown in figure 6.1(b) for ^{85}Rb . The experimental carrier

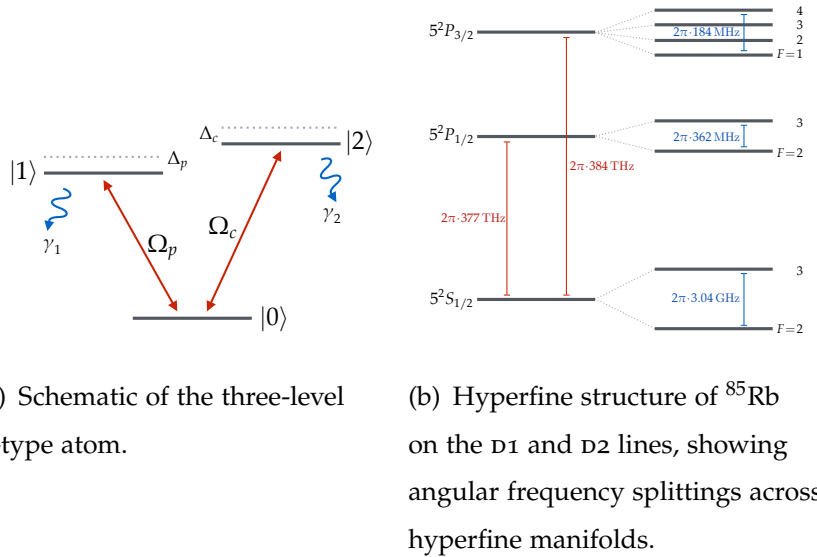


FIGURE 6.1 V configuration level diagrams.

frequencies are tuned resonant with transitions from the $|5^2\text{S}_{1/2} F=3\rangle$ level for ^{85}Rb and so are far-detuned from the other energy level in the doublet. The coupling beam is focused to a waist of $\sim 20 \mu\text{m}$ while the probe beam is focused more tightly to a waist of $\sim 10 \mu\text{m}$, which minimises variation of the coupling intensity for atoms in the probe beam.²⁰

Transmission of the beams through the medium is detected using a fast photodiode with a bandwidth of 8 GHz input to a 12 GHz bandwidth oscilloscope with an effective sampling rate of $\sim 400 \text{ GS/s}$. The oscilloscope is sampling rather than real-time, so the data must be averaged over many cycles. Systematic noise is recorded by taking measurements with the probe laser off and later removing the background from the measured signal.

The cell windows alter the focusing region of the beams, and so spectroscopic measurements are needed to establish accurate Rabi frequencies. The Rabi frequency of the coupling beam atom-light interaction is measured using the Autler-Townes splitting of the ground states. The Rabi frequency of the probe beam is then estimated using the coupling beam

as a guide.

Results were taken over a range of peak intensities for the coupling pulse of 10 to 100 mW and over a vapour temperature range of 200 to 300 °C. In all cases the coupling pulse is shaped to a short Gaussian profile with a FWHM of 0.8 ns. This shaping is performed by a Pockels cell placed between two crossed Glan-Taylor prisms to rapidly rotate the polarisation of the beam.

The experiments were performed and results taken by Kate A. Whitaker and James Keaveney. Further details of the experimental setup may be found in Keaveney, 2013.²⁰

6.2.1 Experimental Results

In figure 6.2 we see an example result for probe field transmission from the experiment described. The change in signal detected is plotted against time. In this case the temperature $T = 200\text{ }^{\circ}\text{C}$ and the cell length $L = 2\text{ }\mu\text{m}$. The coupling pulse has a peak power of 82 mW and is centred at $t = 0$. The coupling pulse plotted is an average of many shots, but there is practically no variation in the pulse shape from shot to shot.

We see the probe transmission peak sharply around 0.5 ns before the maximum of the coupling pulse, which suggests a superluminal propagation effect, perhaps due to a negative refractive index in the medium.²⁵ There is a brief, smaller oscillation before the transmission returns to its original level. The input pulse profile applied in the experiment has an additional ‘bump’ as an artefact of the way the pulse is shaped (this can be seen in the grey pulse shape).

In figure 6.3 we show the recorded change in signal over a range of temperatures from 200 °C to 290 °C. The coupling pulse has a peak optical power of 82 mW and is centred at $t = 0$. For clarity the data has been

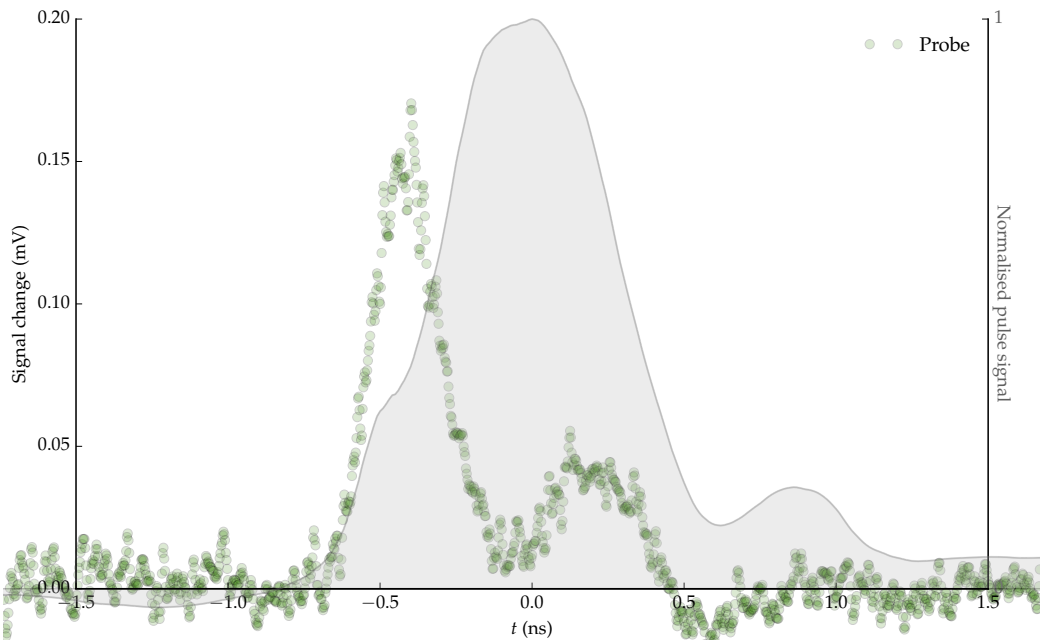


FIGURE 6.2 Recorded probe transmission against time (green circles). The resonant coupling pulse intensity (grey filled area), shown after it has passed through the medium, has a FWHM $t_w = 0.8$ ns, a peak power of 82 mW and is centred at zero. The temperature $T = 200$ °C and the cell length $L = 2 \mu\text{m}$.

smoothed using a moving average with a triangular weighting function.

We see that over the range of temperatures investigated at this power, the steep early response is consistent in time and that the peak of the response increases with temperature in an approximately linear way, with possible saturation of that increase at 290 °C.

In order to understand the distinctive response profile of the signal and determine the physical principles underlying these results, we will now begin building up a theoretical model for the system.

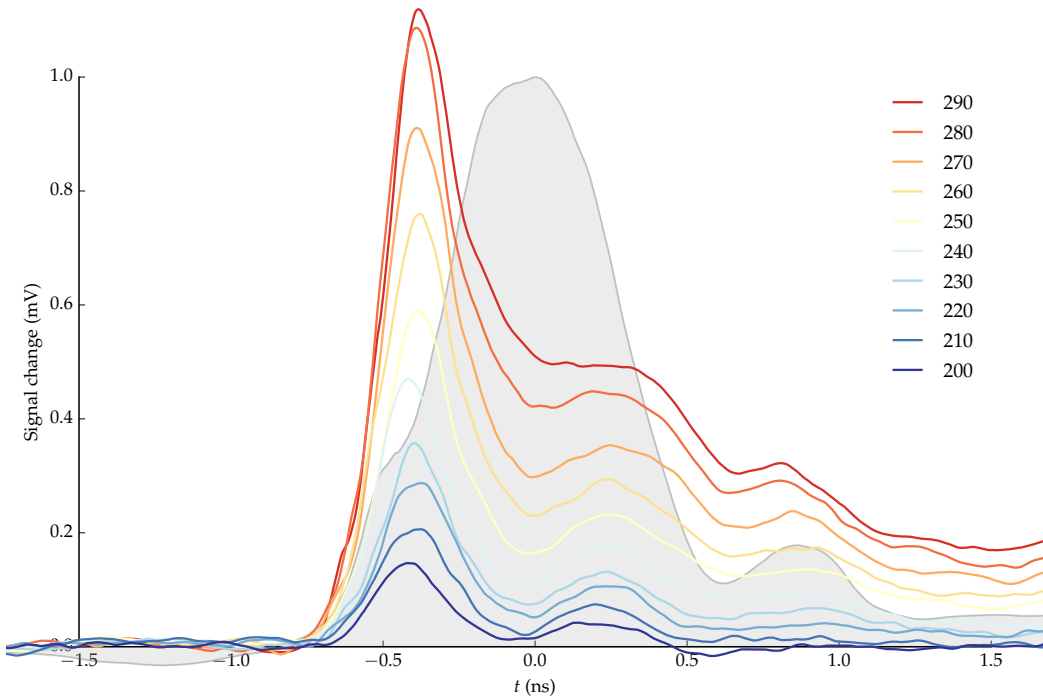


FIGURE 6.3 Recorded probe signal against time (coloured lines) over a range of temperatures from $T = 200\text{ }^{\circ}\text{C}$ to $290\text{ }^{\circ}\text{C}$. The resonant input coupling pulse intensity, shown for the experiment at $T = 200\text{ }^{\circ}\text{C}$ (grey filled area) in each case has a width $t_w = 800\text{ ps}$, is centred at zero and has a peak optical power of 82 mW. The pulse is shown here normalised for time reference.

6.3 Theoretical Model

We start with a quantised three-level atom as illustrated in figure 6.1(a). The probe beam couples the ground state $|0\rangle$ to an excited state $|1\rangle$ while an orthogonal coupling beam couples $|0\rangle$ to an adjacent excited state $|2\rangle$. The transition $|1\rangle$ to $|2\rangle$ is dipole-forbidden, completing the definition of the V-type atom. With this simplified model of the atomic system, we are neglecting the hyperfine structure of the $5^2\text{S}_{1/2}$, $5^2\text{P}_{1/2}$ and $5^2\text{P}_{3/2}$ states. We will discuss this approximation further in section 6.6.

The total electric field vector for the two laser beams is described by

$$\mathbf{E}(z, t) = \left[\frac{1}{2} \hat{\mathbf{x}}_p \mathcal{E}_p(z, t) e^{i(k_p z - \omega_p t)} + \frac{1}{2} \hat{\mathbf{x}}_c \mathcal{E}_c(z, t) e^{i(k_c z - \omega_c t)} + \text{c.c.} \right] \quad (6.1)$$

where $\hat{\mathbf{x}}_p$ and $\hat{\mathbf{x}}_c$ are orthogonal polarisation of the vectors of the fields and the envelopes \mathcal{E}_p and \mathcal{E}_c are in general complex functions. We define corresponding Rabi frequencies $\Omega_p = d_{01}\mathcal{E}_p/\hbar$ and $\Omega_c = d_{02}\mathcal{E}_c/\hbar$ where d_{0j} is the dipole moment between levels $|0\rangle$ and $|j\rangle$, which we take parallel to its respective field polarisation.

The Hamiltonian for the V-type three-level atom interacting with these two classical fields is

$$\mathcal{H}_V = -\hbar(\Delta_p \sigma_{11} + \Delta_c \sigma_{22}) - \frac{\hbar}{2} [(\Omega_p \sigma_{10} + \Omega_c \sigma_{20}) + \text{h.c.}] \quad (6.2)$$

within the dipole approximation and in the frame rotating with the frequencies of the optical fields. Here $\sigma_{ij} := |i\rangle \langle j|$ is the transition operator. Along with accounting for off-resonant fields, the inclusion of detunings Δ_p and Δ_c allows us to consider Doppler broadening via an atom distribution $P(\Delta)$ as described in chapter 2.

Armed with this Hamiltonian we can apply the semiclassical Maxwell-Bloch propagation models described in chapter 2 to solve for the electric fields $\mathcal{E}_{p,c}$ and atomic density operator ρ over z and t as the fields move through the medium.

The temporal profile of the cw probe and Gaussian pulsed coupling input at the front of the medium ($z=0$) constitute the necessary boundary condition on the fields.

Switching on the cw probe field instantaneously from zero to Ω_{p0} would introduce a discontinuity and thus spurious ringing due to the Gibbs phenomenon.¹⁸ We thus construct a switch-on function which

ramps up smoothly. We take a real-valued Ω_p function

$$\Omega_p(z=0, t) = \begin{cases} \Omega_{p0} \exp \left[-4 \log 2 \left(\frac{t-t_0}{t_w} \right)^2 \right] & t < t_0 \\ \Omega_{p0} & t \geq t_0 \end{cases} \quad (6.3)$$

where t_0 is the point at which the function reaches its peak Ω_{p0} . The duration of the ramp-on is governed by t_w , which is the full width at half maximum (FWHM) of a Gaussian. We also require an initial condition for the atomic states, where it is reasonable to assume negligible population in either of the excited states.

The interaction Hamiltonian allows us to follow coherent evolution of pure atomic states. To our analysis we will also include the interaction of atoms with the environment via spontaneous decay of excited states. We'll still be considering coupling pulses much shorter than the decay time associated with this decay as discussed in chapter 3.

The spontaneous decay effect is included in the model via collapse operators C_j in the Lindblad equation (2.29) describing time evolution of the atomic states. For the V configuration atom we have $C_j = \sqrt{\Gamma_{0j}}\sigma_{0j}$ for $j \in \{1, 2\}$ representing spontaneous decay of the excited states, where Γ_{0j} are the decay rates.

6.3.1 Simulation Results

With this theoretical model, we are now in a position to set up and run numerical simulations of the physical system using the Maxwell-Bloch propagation algorithm described in Appendix C.

We present results of an example simulation in figures 6.4, 6.5 and 6.6. In this example we take a rubidium cell of length $L = 2 \mu\text{m}$ at a temperature $T = 230^\circ\text{C}$, which translates to absorption coefficients of $Ng_{01} = 2\pi 66.7 \Gamma/\text{L}$ and $Ng_{02} = 2\pi 128 \Gamma/\text{L}$ (see chapter 2 for a de-

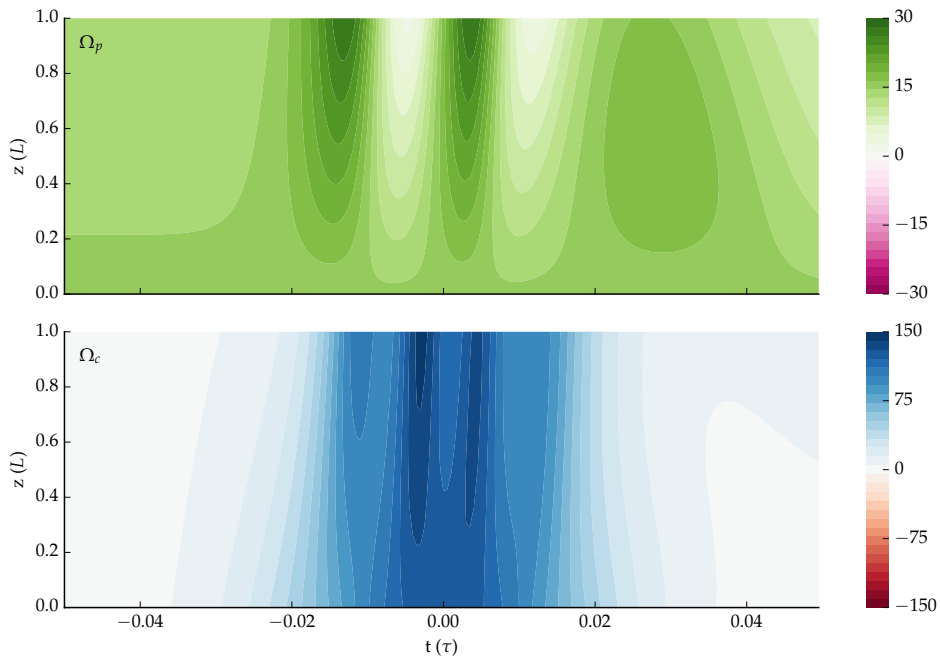


FIGURE 6.4 Real parts of the complex Rabi frequencies Ω_p (top) and Ω_c (bottom) in the simulated pulse/cw scheme. The coupling pulse has width $t_w = 0.029 \tau$ and peak Ω_c of $2\pi 130 \Gamma$. The absorption coefficients are $Ng_{01} = 2\pi 66.7 \Gamma/L$ and $Ng_{02} = 2\pi 128 \Gamma/L$.

scription of the absorption coefficients). Given the decay time $\tau = 1/\Gamma_{01}$, the input ($z = 0$) coupling pulse has a FWHM of $t_w = 0.029 \tau$, (equivalent to 0.80 ns), a peak of $\Omega_c = 2\pi 130 \Gamma$ ($2\pi 748$ MHz) and is centred at $t = 0$. The cw probe is ramped up to $\Omega_p = 2\pi 15 \Gamma$ ($2\pi 86$ MHz) long enough before the pulse (at $t = -1.5 \tau$) for the system to reach a steady state.

In figure 6.4 we look at the evolution of the fields, as described by the real part of the complex Rabi frequencies Ω_p and Ω_c , in the time window around the pulse. The contoured colour maps correspond to the real parts of Ω_p and Ω_c according to the colour scale on the right, with local time t' on the x -axis (these results are displayed in the co-moving reference frame) and the distance z that the fields travel through the medium on the y -axis. The input boundary conditions are thus represented by a horizontal slice at $z=0$.

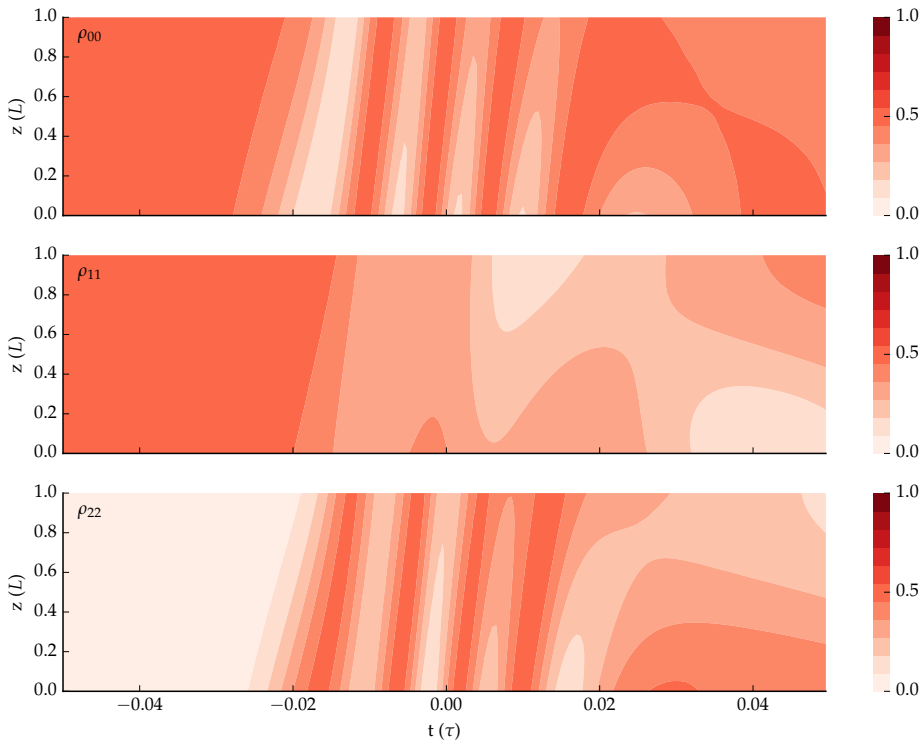


FIGURE 6.5 Populations of the ground state ρ_{00} (top) and excited states ρ_{11} (middle) and ρ_{22} (bottom) over z and t' in the simulated pulse/cw scheme, with parameters as those in figure 6.4.

We see that the coupling pulse (bottom) is not attenuated over this distance, but in fact is shaped and is indeed amplified and split around the centre ($t = 0$). A long-time tail emerges towards the end of the medium ($z = L$).

Before the pulse, the cw probe field (top) is attenuated as it progresses through the medium, as we would expect from the usual Beer law of absorption. This behaviour is abruptly disturbed by the coupling pulse, however. In response to the arriving pulse, the probe field is first amplified over a period of about 0.01τ and then strongly attenuated, and this process repeats twice over the duration of the pulse. After the pulse the field returns to its initial state.

In figure 6.5 we look at the evolution of the atomic populations of the

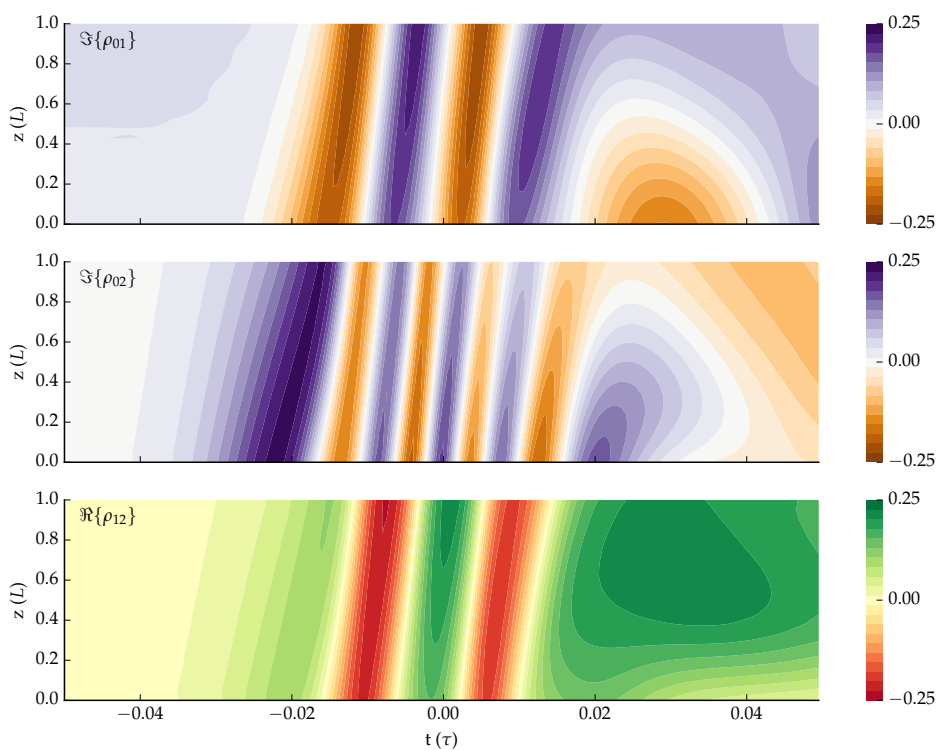


FIGURE 6.6 Selected coherences of the atomic density matrix. The imaginary parts of ρ_{01} (top) and ρ_{02} (middle) and the real part of ρ_{12} (bottom) over z and t' in the simulated pulse/cw scheme, with parameters as those in figure 6.4.

states $|0\rangle$, $|1\rangle$ and $|2\rangle$ during the same window as figure 6.4, with local time t' on the x -axis and the distance z that the fields travel through the medium on the y -axis. These diagonal elements of the density matrix are real and must sum to unity as expressed in equation (A.4), and so the colour scale is from zero to one on each plot.

We see that the population is initially divided evenly between ρ_{00} (top) and ρ_{11} (middle), with no population in the $|2\rangle$ state, as expected since initially the medium is in the steady state driven on resonance by the cw probe field. During the pulse population is driven between ρ_{00} and ρ_{22} (bottom). The population in ρ_{11} is reduced during the pulse. The small positive slope of these features on each of the colour maps shows the pulse arriving later in time relative to the speed-of-light frame as the fields move through the medium. This corresponds to a slow-light refractive index (see chapter 4).

In figure 6.6 we look at the evolution of the off-diagonal density matrix elements during the same window. Some interesting behaviour of the system is demonstrated here. The top two subplots with orange-to-purple colour maps, show imaginary parts of coherences ρ_{01} and ρ_{02} between the ground state and the two excited states. The bottom subplot, with red-to-green colour map, shows the real part of the ρ_{12} coherence between the two excited states, corresponding to phase coherence between these states.

Firstly, we note that the $\Im\{\rho_{02}\}$ coherence (middle) makes around four complete oscillations during the pulse, corresponding to the strong driving field. Secondly, $\Im\{\rho_{01}\}$ (top) makes around two oscillations but out-of-phase with $\Im\{\rho_{02}\}$ such that it is first driven negative. Finally, $\Re\{\rho_{12}\}$ (bottom) is nonzero such that there is a real coherence between the two excited states despite them not being coupled directly. This oscillates on the same timescale as $\Im\{\rho_{01}\}$.

The fact that we see such strong early amplification of the probe field in figure 6.4 suggests that this model includes the cause of the pulse steepening observed in experiment, however there are some important physical mechanisms we should include in order to simulate the system accurately, and we will consider these now.

6.3.2 Inhomogeneous Broadening

As the experiments described in section 6.2 involved thermal atoms, in order to compare these results with our numerical simulations we need to include some important averaging and dephasing effects due to the motion of the atoms.

Due to the Doppler effect the motion of the atoms along the z -axis results in a 1D Maxwell-Boltzmann probability distribution function over detuning^{13, 14}

$$f(\Delta) = \frac{1}{u\sqrt{\pi}} e^{-(\Delta/u)^2} \quad (6.4)$$

where the thermal width $u = kv_w$. Here k is again the wavenumber of the quasi-monochromatic field and $v_w = 2k_B T/m$ is the most probable speed of the Maxwell-Boltzmann distribution for a temperature T and atomic mass m .²⁶

To include this effect in the field propagation equations, as described in chapter 2, we replace the atomic coherence factor by an integral over the convolution of $P(\Delta)$ with the atomic coherence now a function of detuning, so that

$$\frac{\partial \Omega_p}{\partial \zeta}(\zeta, \tau) = iN g_{01} \int_{-\infty}^{\infty} \rho_{01}(\zeta, \tau, \Delta) f(\Delta) d\Delta, \quad (6.5a)$$

$$\frac{\partial \Omega_c}{\partial \zeta}(\zeta, \tau) = iN g_{02} \int_{-\infty}^{\infty} \rho_{02}(\zeta, \tau, \Delta) f(\Delta) d\Delta. \quad (6.5b)$$

6.3.3 Collision Dephasing

We also consider that a thermal cloud of atoms is randomly distributed and that moving atoms will collide with one another. Transient dipole-dipole interactions between colliding atoms leads to a dephasing of dipoles and an additional broadening. We account for this effect by defining a *self-broadening* coefficient β and a parameter known as the Weisskopf radius²⁷

$$r_W = \sqrt{\frac{\beta}{2\pi\bar{v}}} \quad (6.6)$$

where

$$\bar{v} = 2\sqrt{\frac{2}{\pi}}v_w \quad (6.7)$$

is the expected relative speed of a pair of atoms. We may make a *binary approximation*, considering that all collisions involve only two atoms, on the condition that²⁸

$$\frac{4\pi}{3}Nr_W^3 < 1 \quad (6.8)$$

which means that in a sphere around any given atom with a radius r_W , we will expect to find at most one other atom. This dephasing effect is then included via additional off-diagonal decay terms

$$\Gamma_{col,j} = N\beta_j = N\frac{d^2}{3\hbar\varepsilon_0}\sqrt{\frac{2J'+1}{2J+1}} \quad (6.9)$$

where $2J + 1$ and $2J' + 1$ are the fine structure multiplicities of the ground and excited states.^{27,29} Collision broadening thus has the effect of increasing uncertainty in the off-diagonal terms.

For rubidium thermal vapour we have $\beta_{D1} = 2\pi 0.73 \text{ MHz } \mu\text{m}^3$ and $\beta_{D2} = 2\pi 1.03 \text{ MHz } \mu\text{m}^3$ for the D line transitions.²⁹ The binary approximation then breaks down only at a density of $N \approx 10^{17} \text{ cm}^{-3}$ corresponding to a temperature of $T = 360^\circ\text{C}$, and so is a good approximation across the temperature range of the experiment.

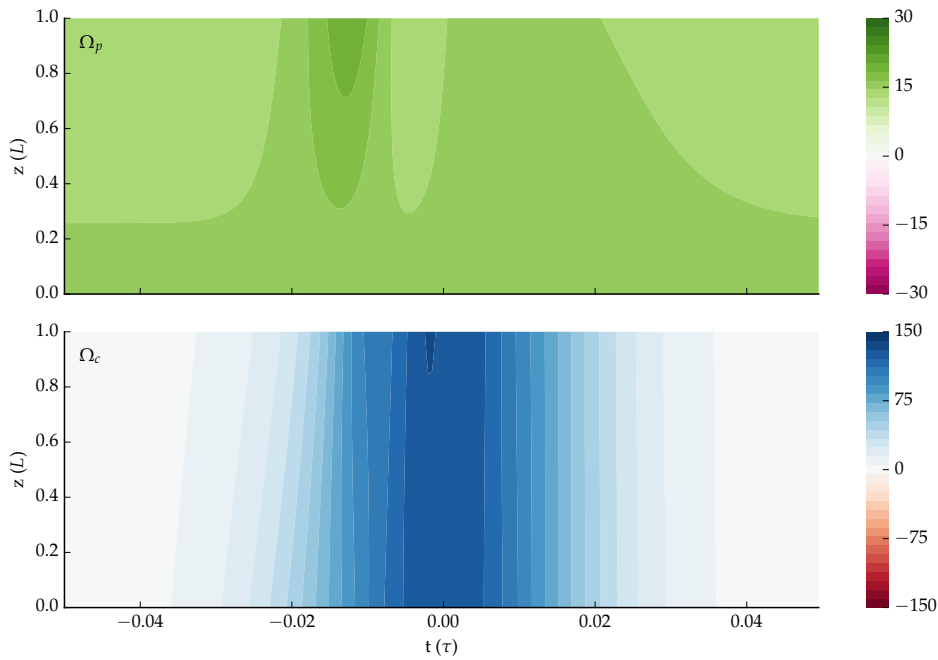


FIGURE 6.7 Real parts of the complex Rabi frequencies Ω_p (top) and Ω_c (bottom) in the simulated pulse/cw scheme for the parameter set in figure 6.4, with the inclusion of motional effects of Doppler and collision broadening.

In figure 6.7 we again show the evolution of the real part of the complex Rabi frequencies Ω_p and Ω_c for the model in figure 6.4, but this time with the inclusion of the motional effects described.

We no longer see the level of amplification and splitting on the coupling pulse that we saw in figure 6.4, with the pulse maintaining its profile through the medium. The strong amplification and attenuation on the cw probe field has also been damped significantly, particularly on the second oscillation. The periods of attenuation return the field Rabi frequency to the level observed without the pulse over this distance.

6.3.4 Hyperfine Pumping

The final physical mechanism we include in our model is that of optical *hyperfine pumping*, which will affect the propagation of both fields.^{30–32}

A rubidium atom with nuclear spin I has two angular momentum values for the ground state: $F = I \pm 1/2$. The hyperfine splitting of this ground state is on the order of GHz, whereas the splitting on the 5P excited states is on the order of MHz, as shown in figure 6.1(b).

If the monochromatic field is tuned to the transition from the lower ground state to the excited state manifold, the higher ground state is far from resonance and so does not couple significantly. The mechanism of decay via spontaneous emission to the higher ground state will then remove atoms from the probe and coupling system.³³

Atoms that have decayed to the lower ground state are *dark* to the optical fields until they are transferred via collision into the higher ground state. The transit time of atoms in the beam is shorter than the timescale of this transfer by collision so the dark ground state is a sink for atomic population, reducing the effective number density and thus absorption of the fields.³⁴

To account for hyperfine pumping, we will add a fourth level as a sink to the three-level system and adjust our initial condition to evenly populate the two ground states. The decay rates Γ_{01} and Γ_{02} to the ground state are then split by branching ratios

$$B_{F \rightarrow J'} = \frac{\sum_{F'} S_{F \rightarrow F'}}{2J' + 1} \quad (6.10)$$

where J, F are the orbital and hyperfine angular momentum numbers for the ground state and J', F' are those of the excited state, and the hyperfine strength factors $S_{F \rightarrow F'}$ are given by³⁵

$$S_{F \rightarrow F'} = (2F' + 1)(2J + 1) \begin{Bmatrix} J & J' & 1 \\ F' & F & I \end{Bmatrix}^2. \quad (6.11)$$

In figure 6.8 we compare results from models with and without the addition of hyperfine pumping to a sink state, for the transmission ob-

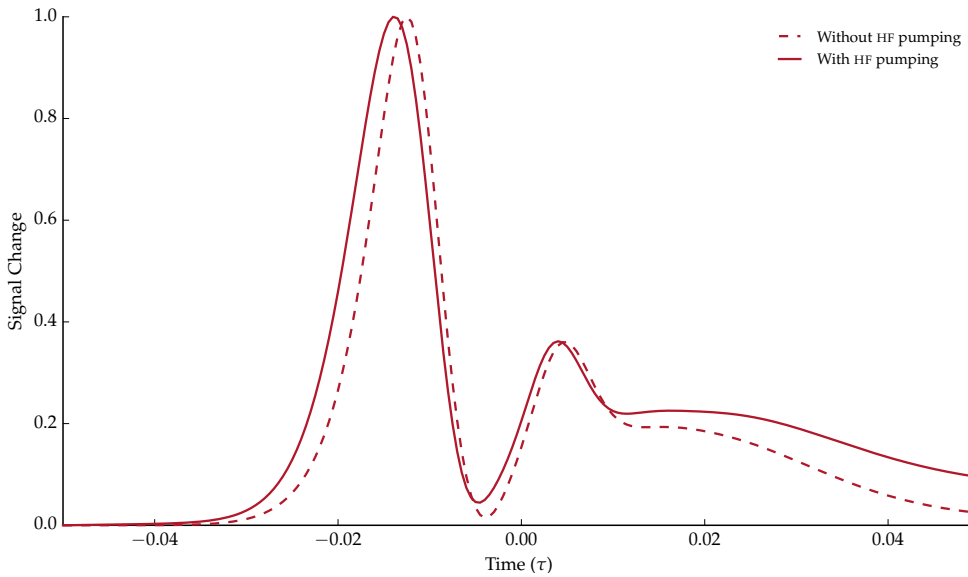


FIGURE 6.8 Simulated transmission intensity at the end of the medium, $z = 1L$ as the probe responds to the input coupling pulse, without hyperfine pumping (red dashed) and with (solid).

served at the end of the medium, $z = 1L$. With the inclusion of pumping, we observe that during the simulation the absorptive power of the medium decreases as population is trapped in the off-resonant dark ground state. This results in an increase in the baseline transmitted signal after the pulse with respect to that beforehand. The peak with the inclusion of HF pumping is slightly earlier, as the slow-light effect of the medium is reduced with the depopulation of the resonant states.

6.4 Comparison of Simulation Results with Data

In the previous section we built up a theoretical model for the physical system, including the significant effects of motion and atomic structure, and presented numerical simulations using parameters matching those of the experiment described in section 6.2. We'll now compare the results of those simulations with the experimental data.

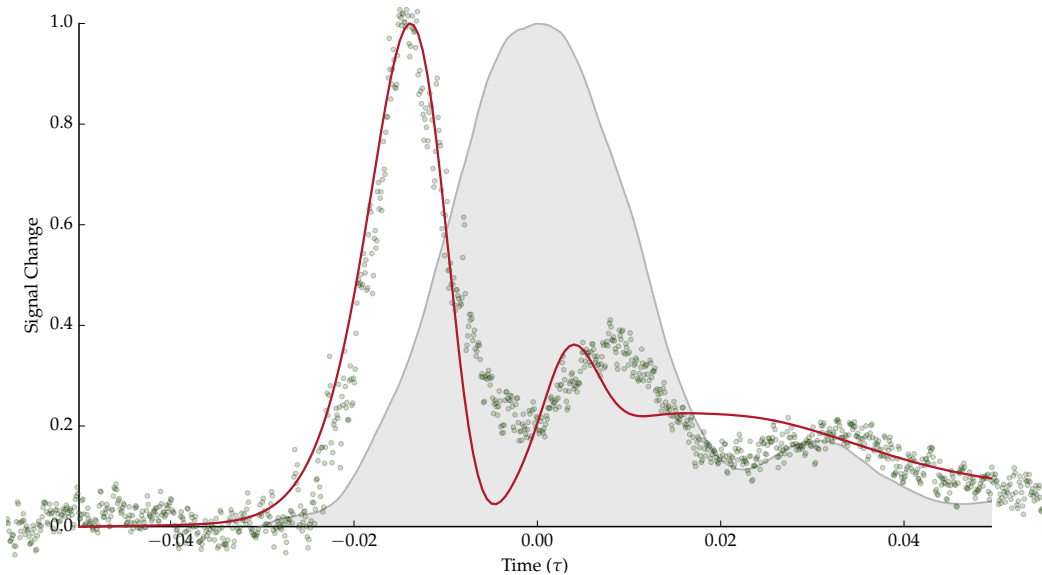


FIGURE 6.9 Comparison of normalised probe transmission profiles from the laboratory data (green circles) and simulation results (red line) for an experiment in the cw/pulse scheme. The measured input coupling pulse intensity (grey filled area) has a width $t_w = 0.80\text{ ns} \equiv 0.029\tau$, a peak power of 85 mW and is centred at zero. In this example $T = 230^\circ\text{C}$ and $L = 2\mu\text{m}$.

In figure 6.9 we present again an example of the response in the probe signal (green circles) as a result of the medium being disturbed by the coupling pulse (grey filled area). In this case the temperature $T = 230^\circ\text{C}$, the length of the vapour cell $L = 2\mu\text{m}$ and the peak pulse power is 85 mW. In contrast to figure 6.2, the probe signal is normalised to unity. Overlaid on the data for comparison this time is the simulation result (red line). The simulated coupling pulse matches the experimental width of $t = 0.029\tau$.

The only fitted parameter in the simulation is the peak Rabi frequency of the coupling pulse envelope. As we shall see when we look at power dependence, the peak Rabi frequency of the coupling pulse determines the arrival time of the signal response. We here use the arrival time of the experimental signal to fit a simulated peak Rabi frequency $\Omega_c = 2\pi 130\Gamma$.

A low-pass filter is applied to the simulation result to account for a limit in resolution of the photon detector of $2\pi \cdot 8$ GHz. This is effected by a Fourier transform of the intensity profile in the time domain to the frequency domain and removal of frequencies $|\omega| > \omega_c$ before an inverse transform is made back to the time domain. A sharp cutoff would introduce discontinuities, so instead we apply a convolution with a roll-off frequency curve

$$f(\omega) = \frac{1}{\sqrt{1 + \left(\frac{\omega}{\omega_c}\right)^2}}. \quad (6.12)$$

We see good qualitative agreement with the data. The simple three-level model result shows the distinctive steep rise in the probe transmission, the early peak around $t = -0.015\tau$ followed by a subsequent, smaller oscillation. The smaller peak arrives early in the simulation, and is narrower than in the data. Both experiment and simulation show the signal returning to its original level beyond $t = 0.04\tau$.

The additional ‘bump’ in the pulse profile is the likely cause of a following oscillation in the probe signal. This artefact is not included in the simulation is not observed in the probe signal tail.

6.4.1 Power Dependence

In figure 6.10 we present results for the probe transmission signal over a range of experimental coupling pulse powers from 20 mW to 100 mW. The input pulse in each case has a FWHM of 0.80 ns, equivalent to $\tau_w = 0.029\tau$ in the natural unit system.

As discussed in section 6.2, the effective probe and coupling Rabi frequencies for the atom-light interaction in the cell is difficult to determine due to the focussing effect of the cell windows. The peak Rabi frequency in the simulation is therefore fitted for that of the 100 mW data,

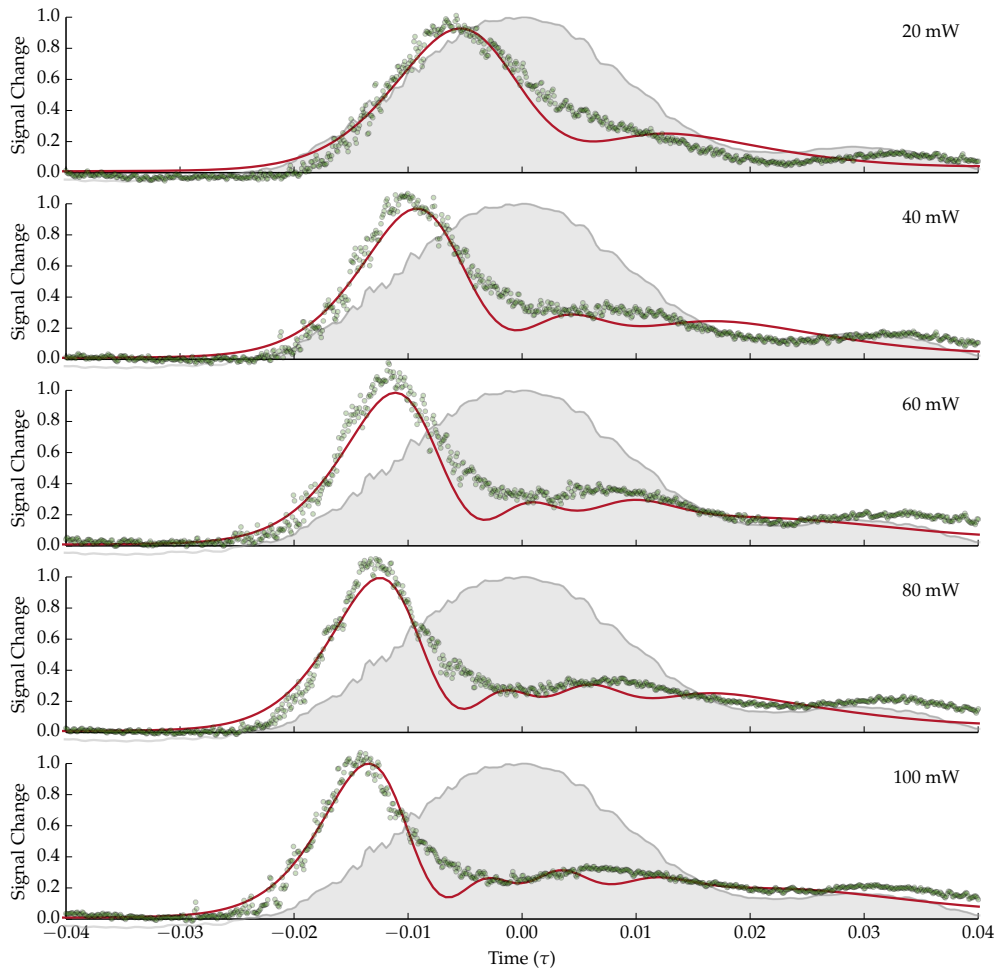


FIGURE 6.10 Comparison of numerical results (red) with experimental data (green circles) for the normalised transmitted probe signal at $L = 2 \mu\text{m}$ over a range of peak coupling pulse powers. The measured coupling pulse signal (grey filled area) has a width $\tau_w = 0.80 \text{ ns} \equiv 0.029 \tau$ in each case, and the 100 mW pulse envelope is shown in each subfigure. The temperature is fixed at 200 °C.

at $\Omega_c = 2\pi 140 \Gamma$. This value is approximately half of that which we calculate directly from the laser power, beam waist and transition dipole matrix element for ^{85}Rb . The difference is reasonable if we take into account our uncertainty in the field amplitude at the site of the atoms due to beam focussing as well as the effective TDME due to hyperfine degeneracy (we will discuss this in section 6.6). The Rabi frequencies for other input intensities are derived from the 100 mW value, following the relationship $\Omega \propto \sqrt{I}$.

The simulation and experimental data are normalised to the peak intensity in response to the 100 mW run. The response peaks at lower powers are reduced in the data, to 0.93 in the 20 mW run. This is matched in the simulation. The key feature of increasing power is to *push the response peak earlier* relative to the coupling pulse, from around -0.08τ for the 20 mW run to -0.15τ for the 100 mW run, and to *steepen* the peaks. The simulation results also match this behaviour over the power range investigated.

6.4.2 Temperature Dependence

In figure 6.11 we present numerical results for the probe transmission signal in the time window around the pulse ($t = 0$) over a range of temperatures from 200 °C to 282 °C. These simulated results are shown on top of the experimental data for comparison, and the measured coupling pulse for each run is shown (normalised) for reference on the time axis.

We see that there is good qualitative agreement between the simulated result and experimental data across the temperature range. The increase in temperature does not significantly affect the peak time of the response signal, but does linearly increase the peak intensity, and this is

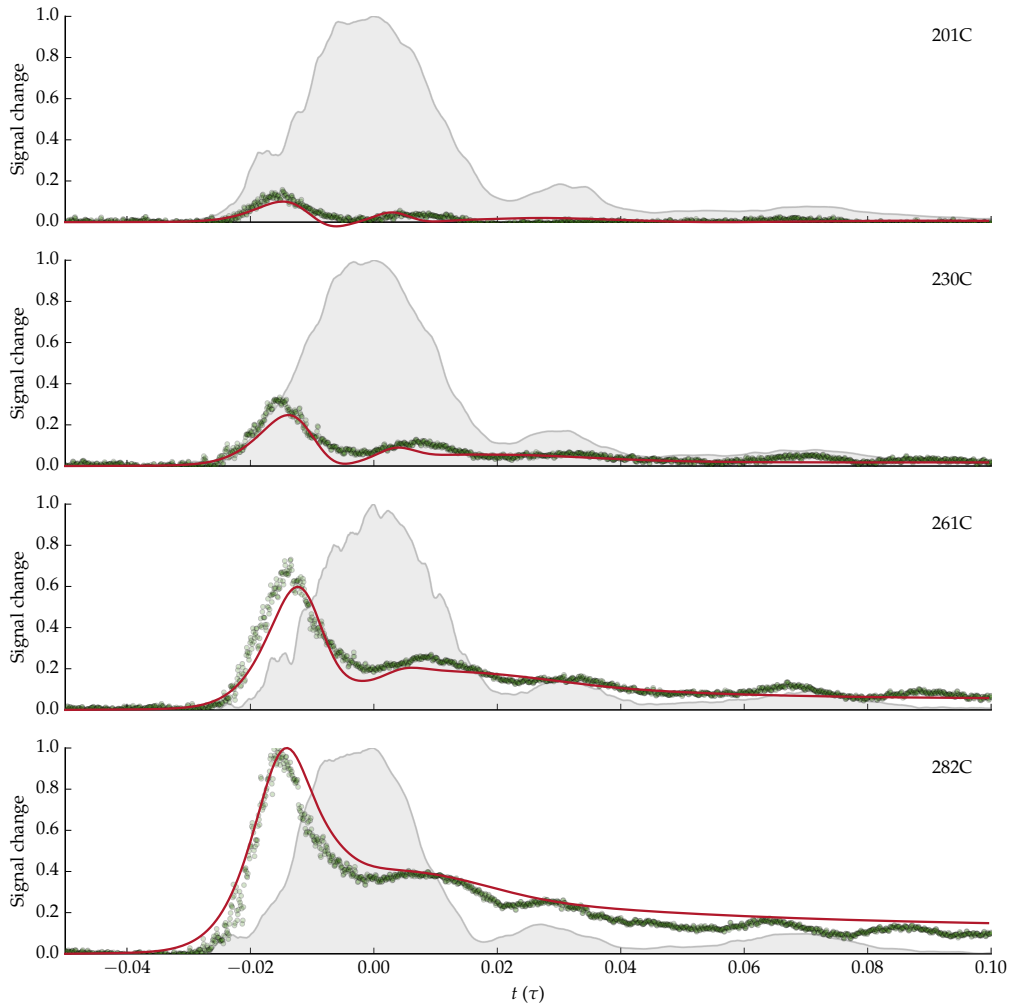


FIGURE 6.11 Comparison of numerical results (red) with experimental data (green circles) for the transmitted probe signal at $L = 2 \mu\text{m}$ over a range of temperatures from 200 °C to 282 °C. The signals are normalised to the peak of the 282 °C data. The normalised measured coupling pulse signal (grey filled area), shown for comparison, has a width $\tau_w = 0.80 \text{ ns} \equiv 0.029 \Gamma$ in each case. The coupling pulse power is 85 mW.

matched in the simulation. The behaviour of the probe after the pulse has passed is also in reasonable agreement, though there are clear oscillations in the data which are not matched in the simulation.

6.4.3 A Recap

At this point we have built up a theoretical model based on propagation of the fields through a V-type three-level medium, considering important physical effects of inhomogeneous broadening, binary collisions and hyperfine pumping. We've chosen appropriate parameters to compare simulation results with the experimental data and observe a good qualitative fit across the power and temperature parameter space covered in the laboratory study.

Having some trust that our model is useful in matching the experiment, we'd like to gain physical insight into the underlying mechanisms responsible for the observed data. We begin by looking more closely into the response of an individual atom to the applied fields.

6.5 Analysis of the Evolution of a Single Atom

In order to understand the steep, early response in the cw probe signal observed in the experiment and matched in the numerical simulations, we turn in this section from the fields to focus on the evolution of the density matrix of a single atom as it is addressed by the probe and subsequently disturbed by the coupling pulse.

As discussed in appendix A, the density matrix ρ is used to describe the state of an open quantum system such as an atom interacting both with coherent fields and with a stochastically modelled environment. We follow the evolution of ρ using the Lindblad master equation (A.8).

The Hamiltonian for the V-type atom was given in equation (6.2). In the case of the pulsed coupling scheme, at the front of the medium we have input time-dependent fields $\Omega_p(t)$ and $\Omega_c(t)$ and thus a time-dependent Hamiltonian $\mathcal{H}_V(t)$. We can solve the Lindblad equation numerically given an initial condition.

We imagine the cw probe having plenty of time to equilibrate before the pulse, so we first find the steady state solution with the probe on and the coupling pulse off. This steady state constitutes the initial condition.

In figure 6.12 we show the time evolution of density matrix populations and coherences for an example Gaussian pulse profile of peak 100Γ and width $0.02\tau_\Gamma$, where here we'll assume $\Gamma := \Gamma_{01} = \Gamma_{02}$ and define $\tau_\Gamma := 1/\Gamma$ as the reciprocal lifetime. The cw probe Rabi frequency is 50Γ . Before the pulse, the steady state population is an even split between ρ_{00} and ρ_{11} . As the pulse ramps on we see it coherently drive population transfer such that it oscillates between populations ρ_{11} and ρ_{22} . This is accompanied by a positive real coherence ρ_{12} , and an imaginary coherence ρ_{01} which oscillates first negative and then positive. After the pulse we see damped oscillation of ρ_{00} and ρ_{11} , and at long times we expect the system to return to its steady state.

The behaviour of the imaginary part of ρ_{01} is of particular interest as we know that the macroscopic consequence of this atomic coherence is polarisation of the medium with respect to the probe field, and resulting attenuation or amplification of that field. From the observed evolution we can then predict that during the pulse, without the populations $|0\rangle$ and $|1\rangle$ being inverted, we will find reduced absorption and possibly gain in the probe field.

To understand this time evolution, we write out the components of equation (2.29) for the V configuration to get a set of differential equa-

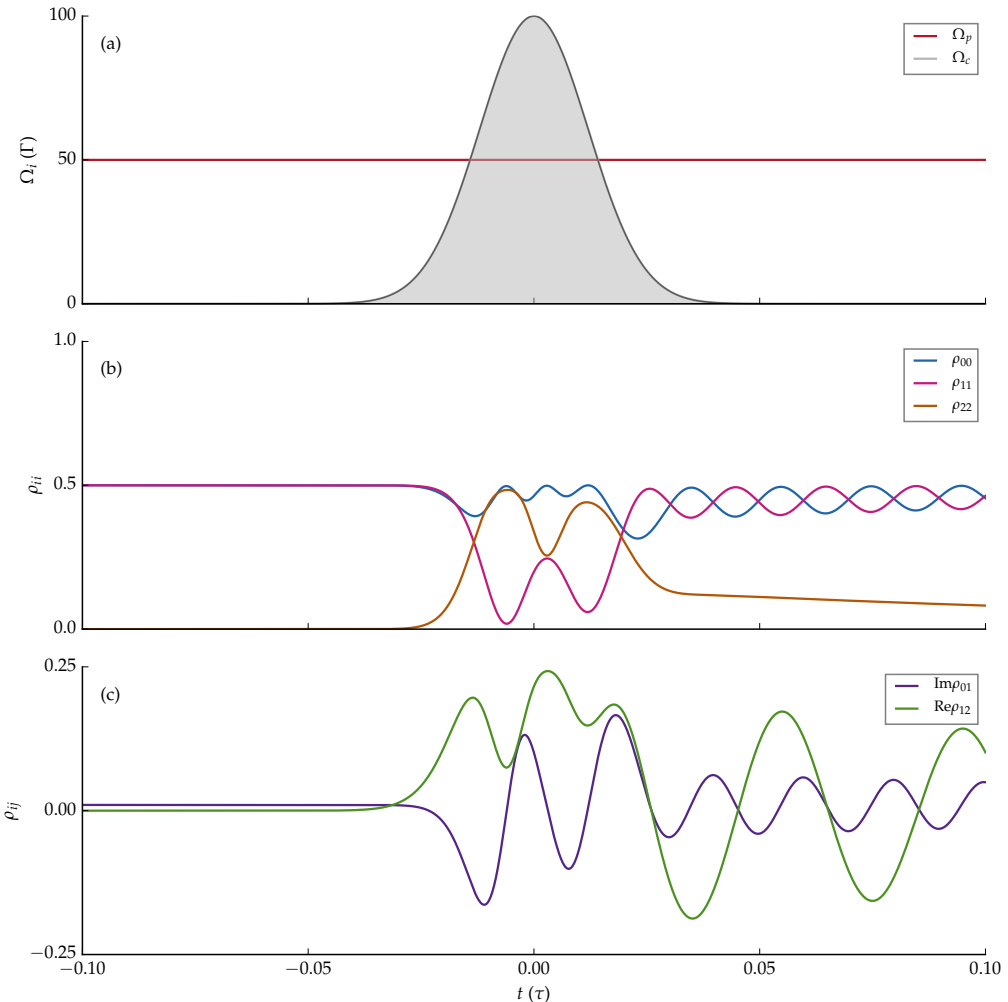


FIGURE 6.12 Time evolution of the density matrix elements from numerical solution of the master equation for the V configuration atom. (a) Rabi frequency profiles of the two fields: a cw probe Ω_p (red) and Gaussian pulsed coupling Ω_c (grey) with amplitude $2\pi \times 100\Gamma$ and width $t_w = 0.02\tau_\Gamma$. (b) Populations of the atomic eigenstates. (c) The imaginary part of coherence ρ_{01} (purple) and the real part of coherence ρ_{12} (green).

tions for the density matrix elements

$$\frac{\partial \rho_{00}}{\partial t} = \Gamma_{01}\rho_{11} + \Gamma_{02}\rho_{22} + \frac{i}{2} \left[\Omega_p(\rho_{01} - \rho_{10}) + \Omega_c(\rho_{02} - \rho_{20}) \right] \quad (6.13a)$$

$$\frac{\partial \rho_{01}}{\partial t} = -\frac{\Gamma_{01}}{2}\rho_{01} - i\Delta_1\rho_{01} + \frac{i}{2} \left[\Omega_p(\rho_{00} - \rho_{11}) - \Omega_c\rho_{21} \right] \quad (6.13b)$$

$$\frac{\partial \rho_{02}}{\partial t} = -\frac{\Gamma_{02}}{2}\rho_{02} - i\Delta_2\rho_{02} + \frac{i}{2} \left[-\Omega_p\rho_{12} + \Omega_c(\rho_{00} - \rho_{22}) \right] \quad (6.13c)$$

$$\frac{\partial \rho_{11}}{\partial t} = -\Gamma_{01}\rho_{11} - \frac{i}{2}\Omega_p(\rho_{01} - \rho_{10}) \quad (6.13d)$$

$$\frac{\partial \rho_{12}}{\partial t} = -\frac{\Gamma_{01}}{2}\rho_{12} - \frac{\Gamma_{02}}{2}\rho_{12} + i(\Delta_1 - \Delta_2)\rho_{12} - \frac{i}{2}(\Omega_p\rho_{02} - \Omega_c\rho_{10}) \quad (6.13e)$$

$$\frac{\partial \rho_{22}}{\partial t} = -\frac{\Gamma_{02}}{2}\rho_{22} - \frac{i}{2}\Omega_c(\rho_{02} - \rho_{20}). \quad (6.13f)$$

Note that $\rho_{10} = \rho_{01}^\dagger$ and $\rho_{20} = \rho_{02}^\dagger$.

Starting with equation (6.13e) we see that in the case of two-photon resonance ($\Delta_1 = \Delta_2 = 0$) and in the steady state at the start of the pulse

$$\frac{\partial \rho_{12}(t_0)}{\partial t} \approx \frac{i}{2}\Omega_c(t_0)\rho_{10}(t_0). \quad (6.14)$$

The steady state ρ_{10} for the two-level system is positive imaginary, thus ρ_{12} is initially driven real and positive by the pulse.

If we next look at equation (6.13b), we see that again on resonance and in the steady state with $\rho_{11} = \rho_{00}$

$$\frac{\partial \rho_{01}(t_0)}{\partial t} \approx -\frac{i}{2}\Omega_c\rho_{21} \quad (6.15)$$

such that with ρ_{21} real and positive ρ_{01} is driven imaginary and negative. This is consistent with the behaviour observed in the evolution of coherences in figure 6.12.

6.5.1 Coherent Population Trapping

We may gain further insight into the transient effect of the pulse on the system by considering the eigenstates of the atom dressed by the fields,

that is the eigenvectors of \mathcal{H}_V .^{4,36} If we consider equal detunings $\Delta := \Delta_p = \Delta_c$ and solve for $\mathcal{H}_V |\psi\rangle = \hbar\lambda |\psi\rangle$ we find eigenvalues

$$\lambda_0 = -\Delta \quad (6.16a)$$

$$\lambda_{\pm} = \frac{-\Delta \pm \bar{\Omega}}{2} \quad (6.16b)$$

where $\bar{\Omega} = \sqrt{\Omega_p^2 + \Omega_c^2 + \Delta^2}$. These eigenvalues have corresponding normalised eigenstates

$$|D\rangle = \frac{1}{\sqrt{N_0}} (-\Omega_c |1\rangle + \Omega_p |2\rangle) \quad (6.17a)$$

$$|B_{\pm}\rangle = \frac{1}{\sqrt{N_{\pm}}} (-2\lambda_{\mp} |0\rangle + \Omega_p |1\rangle + \Omega_c |2\rangle) \quad (6.17b)$$

where $N_0 := \Omega_p^2 + \Omega_c^2$ and $N_{\pm} := N_0 + 4\lambda_{\mp}^2$.

Note that the energy eigenvalue λ_0 is zero on resonance, such that it is decoupled from the fields. For this reason, its corresponding eigenstate $|D\rangle$, which does not contain any component of the ground state, is known as a dark state. Any population entering the dark state cannot be driven out again by the coherent fields, it can only decay spontaneously. This phenomenon is known as coherent population trapping (CPT).³⁷ The states $|B_{\pm}\rangle$, which are coupled to the fields, are known as bright states.

We can transform from the bare state density matrix ρ to the similar CPT state density matrix ρ' via

$$\rho' = \mathcal{T}^{-1} \rho \mathcal{T} \quad (6.18)$$

where \mathcal{T} is the unitary transform defined by equations (6.17).

In figure 6.18, we show the time evolution of the populations of the CPT states $|D\rangle$ and $|B_{\pm}\rangle$ during the pulse shown in figure 6.12 for the bare states. We see that during the pulse, a significant amount of population is driven into the dark state $|D\rangle$, where it will be trapped. This suggests the effects of the pulse will be counteracted after a short time period.

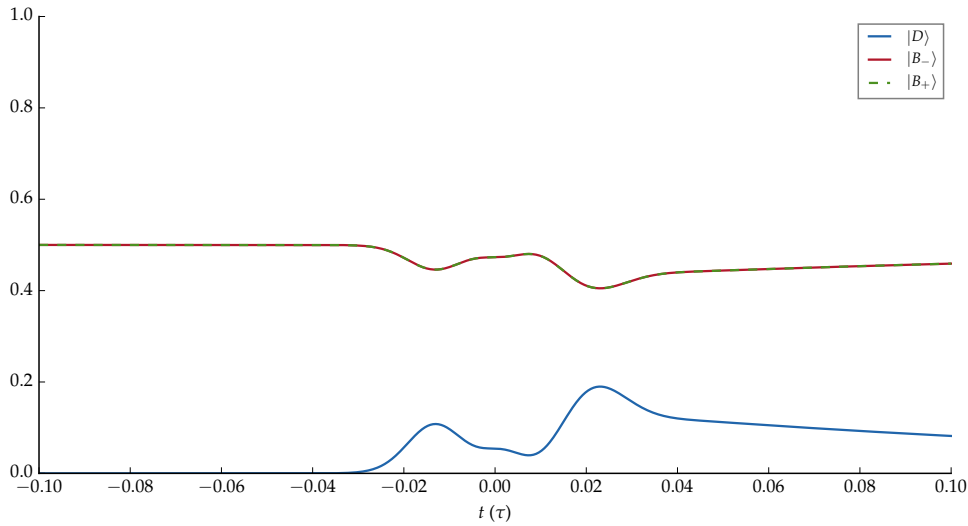


FIGURE 6.13 Time evolution of the populations of the CPT state populations $|D\rangle$ (blue), $|B_-\rangle$ (red) and $|B_+\rangle$ (green dashed) for the V-type atom addressed by a coupling pulse with amplitude 100Γ and width $t_w = 0.02\tau_\Gamma$.

In summary, in this section we have analysed the time evolution of the atomic states in both the bare and CPT basis during the pulse. We found that the strong pulse drives an oscillation, first negative, in the imaginary part of ρ_{01} , which we expect to cause a reduction in absorption or even amplification of the probe beam due to the relation of this coherence to the macroscopic polarisation of the medium.

Looking at the CPT basis, we also find that the pulse results in population trapping in the dark state, which does not interact with the fields, and so we expect the reduction in absorption to be short-lived.

These findings are consistent with the observed signal increase in the probe beam during the early part of the pulse. It does not, however, explain the increase in the signal response with increased temperature. For a complete understanding of the behaviour, we will next move on to considering the effects of pulse propagation and investigate what would happen if we extend the simulations to longer propagation distances.

6.6 Simulating Longer Propagation Distances

Thus far we have considered the behaviour of the atomic medium as addressed by the cw probe and disturbed by the strong pulse over the propagation distance of the thin cell. The restricted propagation distance is a limit of the current experimental setup, but in our numerical simulations we are not subject to the same constraint. We may extend the propagation medium arbitrarily far to observe what happens to both the atoms and the propagating fields. This will complete our analysis of the observed signal response, and also allow us to make predictions for future laboratory studies.

6.6.1 Propagation in the Coupling Pulse Scheme

We will first consider some demonstration cases, before looking at the specific parameters for the experimental system. We know from the study of two- and three-level media in chapter 3 that a key property in the propagation of short pulses in nonlinear systems is the pulse area θ defined in equation ???. Thus we'll design simulations with fixed input pulse areas, rather than specifying the peak intensities as we have done so far. Of course, for a given Gaussian pulse width, these definitions are interchangeable.

We will for now neglect the motional and hyperfine pumping effects we added to the model in section 6.3, as we seek to gain physical insight into the specific effects of propagation.

In figure 6.14 we present numerical results for the cw probe, coupling pulse scheme in a medium with absorption coefficients set at $Ng_{01} = Ng_{02} = 2\pi 10^3 \Gamma/L$. This is an order of magnitude larger than those representing the thin cell experiments, and therefore represents a longer

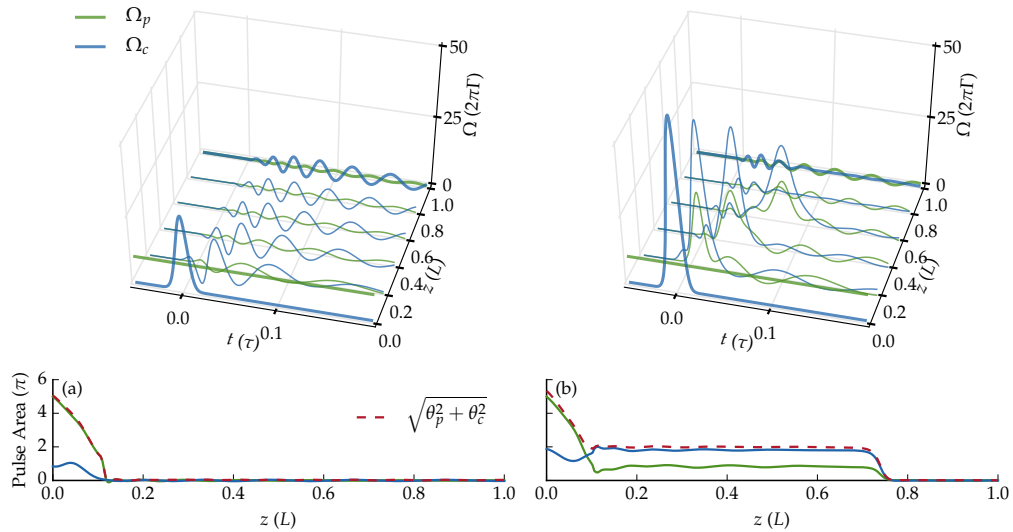


FIGURE 6.14 Propagation of (a) 0.8π and (b) 1.8π coupling pulses (blue) through a medium addressed by a 10Γ cw probe (green), showing (top) profiles of the real part of the complex Rabi frequencies $\Omega(z, \tau)$ and (bottom) pulse areas $\theta(z)$.

distance of propagation. The coupling input pulses are Gaussians of width $\tau_w = 0.01\tau_\Gamma$ and have pulse areas of (a) 0.8π (corresponding to a peak $\Omega_c = 2\pi 28\Gamma$) and (b) 1.8π (a peak $\Omega_c = 2\pi 62\Gamma$). In both cases the cw probe is strong with Rabi frequency $\Omega_p = 2\pi 10\Gamma$.

In figure 6.14(a) we see that for the 0.8π pulse both the cw probe and the coupling pulse are absorbed close to the front of the medium, with the pulse area dissipated by around $z = 0.1L$. From then on the only remnant of the fields is the fast ringing.

In figure 6.14(b) we see that for the 1.8π pulse, the large coupling pulse kicks up a pulse from the cw field, consistent with our analysis of a period of reduced absorption. Of interest in this long distance simulation is that the resultant probe pulse is able to form its own steady-state soliton, as described in the study of matched pulses in chapter 3. Rather than dissipating entirely, the probe pulse area θ_p (bottom, green) is held abruptly at around $z = 0.1L$ to a value of around 1π . The simultane-

ous propagating pulses first steepen toward the sech shape, but then broaden and slow due to the spontaneous decay. We see the large area of the cw probe decreases but doesn't disappear, and the combined pulse area $\theta = \sqrt{\theta_p^2 + \theta_c^2}$ (bottom, red dashed) finds its steady state at 2π . The pulses do not reach the end of the medium in the duration of the simulation, propagating a distance of $z = 0.7L$.

We may ask: what does it mean to define a pulse area for an input cw field? For our purposes, we may take it to be arbitrarily large. Numerically, we integrate the Rabi frequency envelope over the duration of the simulation. The key point is that in the case that the combined pulse area is large enough to support simultaneous propagation, this arbitrarily large pulse area does not dissipate but is held.

What happens for stronger pulses? In figures 6.15 and 6.16 we present results for larger-area pulses input on the same medium with the same cw probe field of $\Omega_p = 10\Gamma$. The coupling input pulses are again Gaussians of width $\tau_w = 0.01\tau_\Gamma$.

In figure 6.15, for the 4.5π pulse, we see the coupling pulse break apart as we've seen previously. Again we see that the pulse kicks up a simultaneous pulse in the probe field as the absorption is initially reduced, which allows a small pulse area to move through, and this is carried on by the first resultant 2π pulse.

We may understand the reason that only one pulse propagates in the probe field by considering the evolution of the off-diagonal matrix elements we presented in figure 6.6. For every two oscillations in ρ_{02} , the system evolves through one oscillation in ρ_{01} . This oscillation forms the probe component of a pulse that matches with the first coupling pulse and propagates as a simulton.

In figure 6.16, for the 6.5π pulse, we see that the coupling pulse breaks

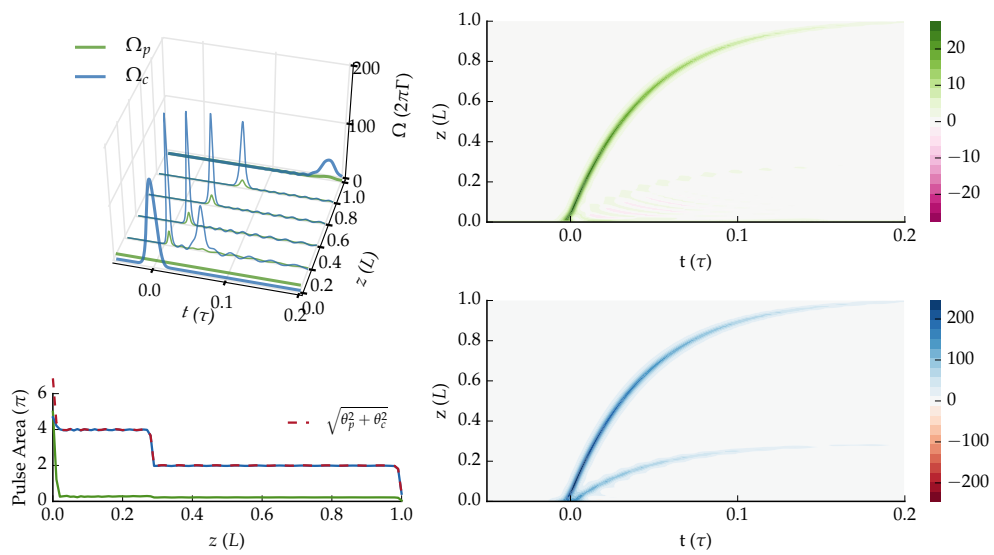


FIGURE 6.15 Propagation of a Gaussian 4.5π input coupling pulse with width $0.01\tau_F$ through a V-type medium addressed by a 10Γ cw probe. (Top left) Propagation profile of the probe (green) and coupling (blue) fields. (Bottom left) Pulse areas of the fields and the total area (red dashed). (Right) Colourmaps of the real part of the complex Rabi frequencies Ω_p and Ω_c .

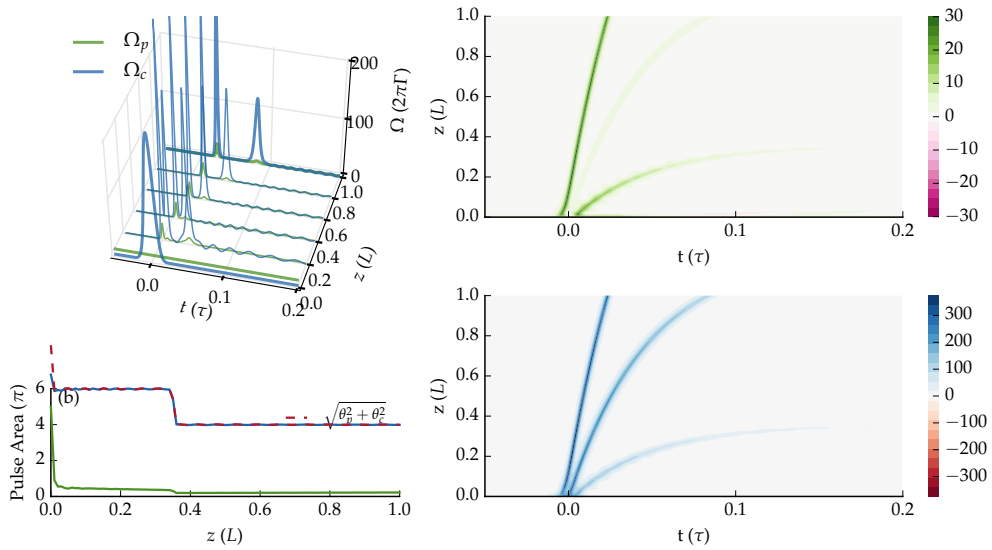


FIGURE 6.16 Propagation of a Gaussian 6.5π input coupling pulse with width $0.01\tau_T$ through the V-type medium addressed by a 10Γ cw probe. (Top left) Propagation profile of the probe (green) and coupling (blue) fields. (Bottom left) Pulse areas of the fields and the total area (red dashed). (Right) Colourmaps of the real part of the complex Rabi frequencies Ω_p and Ω_c .

into three resultant pulses as we'd expect and the kicked up pulse area in the probe field is carried mostly by the first and third resultant 2π pulses.

These demonstrative simulations provide an interesting result: a portion of the cw probe field is in fact picked up by the strong pulse and carried along as one or more simultaneous pulses with the same width, at the same velocity, and capable of propagating over long distances.

6.6.2 Comparison with Experimental Data

The discovery that a strong coupling pulse has the effect of causing a long-distance propagating soliton in the cw probe leads us to consider the experimental results from the thin cell, using the parameters of section 6.2, but imagining that the cell is longer. Recall that in the case of

transitions on the the rubidium D1 and D2 lines we have distinct values for g_{01} and g_{02} , as they are proportional to the square of the respective dipole moments, d_{0j}^2 . This may affect the ability of the pulses to match and propagate.

In figure 6.17 we present again the comparison of numerical result and experimental data shown in figure 6.9. In the experiment the temperature $T = 230^\circ\text{C}$, and the peak pulse power is 85 mW, and the same parameters are simulated. We again present the real part of Ω_p and Ω_c but continue the simulation over a longer distance, imagining that the cell is much longer at $50 \mu\text{m} \equiv 25 L$. This will allow us to predict the long-distance behaviour.

The coupling pulse has a large pulse area $\theta_c = 9.1\pi$, and so over the longer distance we start to see the same pulse break-up we saw in figures 6.15 and 6.16. Again it is the earliest resultant pulse which carries along a pulse in the probe field, rising before the centre of the pulse at $t = 0$. The later resultant pulses in the coupling field are unable to propagate far into the medium due to the dephasing effect of collision broadening.

The simulated result of the field propagation over longer-distances thus gives us an understanding of the mechanism behind the observed transmission profiles in the probe field when the system is disturbed by the strong coupling pulse. We see that *it is the formation of this nascent soliton* in the probe field which causes the steep early in the experimental signal as the probe field is shaped towards a sech-shaped soliton.

It also explains why the peak intensity increases with temperature and number density as observed in figure 6.11, as we are in the nascent stage when the pulse is being shaped. We expect it to saturate as the sech-shape reaches its steady state, and this may be what we see in figure 6.3 at the highest temperature investigated of $T = 290^\circ\text{C}$.

6.6.3 Hyperfine Structure & Degeneracy

A complete account of the electronic energy level structure of rubidium would include fine and hyperfine structure, as considered for the model in chapter 5. Approximating the rubidium vapour as a three- or four-level atomic medium appears to be justified here on the basis that the simulated transmission profiles provide a good qualitative fit to the data along with physical insight into the underlying coherent mechanism.

The discovery, however, that pulse propagation effects are significant means that the physical structure of the atomic energy levels requires further consideration. This is clear if we consider the pulse area, introduced in chapter 3, which is given by

$$\Theta(z) = \int_{-\infty}^{\infty} \Omega(z, t) dt = \frac{d}{\hbar} \int_{-\infty}^{\infty} \mathcal{E}(z, t) dt. \quad (6.19)$$

This quantity is well-defined only if the atomic levels coupled have a uniquely specified dipole moment d . We understand that the physical system in fact has this deeper hyperfine structure due to coupling of the electron's orbital angular momentum L , spin S and the nuclear spin I , as shown in figure 6.1(b). An additional concern is that, in the absence of an applied magnetic field, the $2F + 1$ sublevels of these hyperfine F levels are spatially degenerate such that there is no straightforward way for these m_F states to be addressed separately.

The couplings between these degenerate sublevels will then have different dipole matrix elements $\langle Fm_F | \mathbf{e}\mathbf{r} | F'm'_F \rangle$ and therefore different Rabi frequencies Ω , and this can be expected to suppress the formation of coherent optical solitons.

However, in the case of the experimental study of this chapter, the shortness of pulse duration is such that its spectral width is on the order of $\sim 2\pi 1 \text{ GHz}$. The hyperfine manifolds of the $5^2P_{1/2}$ and $5^2P_{3/2}$ levels are

spread over an energy range on the order of $\sim 2\pi 100 \text{ MHz}$, so the pulse interacts with the full manifold of excited state hyperfine levels $J \rightarrow J'$, and this excited hyperfine structure is not accessible.

Taking just a single $J \rightarrow J'$ transition for now, the effective dipole moment for a particular ground state sublevel $|Fm_F\rangle$ is then found by summing the coupling to all of these excited state sublevels. In general for $J = 1/2$,³⁸ and in the case of linearly-polarised light coupling levels such that the angular momentum difference $q = m'_F - m_F = 0$, we have³⁵

$$\sum_{F'} (2F' + 1) (2J + 1) \left\{ \begin{matrix} J & J' & 1 \\ F' & F & I \end{matrix} \right\}^2 |\langle F m_F | F' 1 m_F 0 \rangle|^2 = \frac{1}{3} \quad (6.20)$$

independent of the particular values of F and F' such that the effective dipole moment is given by

$$d = \sqrt{\frac{1}{3}} \langle J || e\mathbf{r} || J' \rangle. \quad (6.21)$$

for *every* sublevel $|Fm_F\rangle$, where $\langle J || e\mathbf{r} || J' \rangle$ is the reduced dipole operator for the fine structure transition, which is known experimentally from the natural linewidth.

This factor of $\sqrt{1/3}$ can be understood as due to spherical symmetry, by considering that the linearly polarised light will interact with only one of the spherical components of the dipole operator.

Then what about the orthogonal, linearly-polarised beam? As we have defined the first transition to be the π ($q = 0$) transition, the orthogonal beam is defined by a polarisation vector $(\sigma_+ + \sigma_-) / \sqrt{2}$, a symmetric combination of photons either adding or subtracting a quantum of angular momentum to the atom. By making a summation as in equation (6.20) for the $q = 1, -1$ transitions, we find the same $1/\sqrt{3}$ factor, which we would expect again by considering the symmetry of the system.

The result is then for the system to respond as if there were indeed a

unique dipole moment, but one which must take into account the symmetry factor in equation (6.21) and we are justified in applying the simple three-level model.

6.6.4 Weak Probe Fields

Thus far we have considered examples of propagation in the cw probe scheme in which the field is strong. Such strong fields were required in the experiment in order to achieve good detection on the fast photon counter employed. Theoretically, however, we are inclined to consider weak pulses as they may be useful in applications such as quantum information processing and storage.

As described in chapter 3, the pulse area theorem in the case of three-level V-type systems applies not to the individual pulse areas, but to their sum in quadrature. This suggests that if the coupling pulse applied on the adjacent transition is strong, we may be able to consider the scheme for propagation of weak probe through a medium to which it would normally be opaque.

In figure 6.18 we present numerical results which indicate that this is indeed the case. The input Gaussian has a pulse area of 2.2π , while the cw probe field has a Rabi frequency of only 0.001Γ .

Before the pulse, the probe field is absorbed immediately by the medium. We see that as for the strong probe field, the coupling pulse allows transmission of the probe field. We observe that this weak probe, despite being weak enough to excite only a tiny fraction of the atomic population to the ρ_{11} state, is able to propagate simultaneously with the coupling pulse just as the strong probe was. The three-level pulse area is nearly all in the coupling field, but the induced pulse in the probe field is not attenuated as it would be were the coupling field not present.

Some high-frequency ringing is seen in the probe field.

Figure 6.19 shows the populations of the atomic states. We see propagation of a 2.2π Gaussian input coupling pulse with width that the propagation of the induced pulse in the probe field occurs despite negligible population transfer to the $|1\rangle$ excited state. The population is nearly entirely transferred from the ground state $|0\rangle$ to the $|2\rangle$ excited state.

6.7 Discussion

The results presented early on in this chapter, from experiments on a thermal vapour of rubidium atoms addressed by two co-propagating lasers in a vee-type scheme, are certainly intriguing. Over a range of temperatures and powers we observe an early, steep peak in response of the cw probe on the D1 transition when disturbed by a strong, short pulse on the D2 transition.

In order to understand this response behaviour, we designed a theoretical model for the system based on a three-level Maxwell-Bloch description for semiclassical propagation. We included significant physical effects of inhomogeneous Doppler broadening, dephasing due to collisions between moving atoms and hyperfine pumping to a far-detuned state in the ground state doublet. This simple model provides a good qualitative fit to the data over the range of temperatures and powers investigated experimentally, accounting for the peak times of the response relative to power and the relative height of the peak relative to atomic density.

By considering the behaviour of a single atom addressed by the co-propagating fields, both in the bare atomic state basis and the coherent population trapping (CPT) basis, we gain important physical insight

into the transient reduction of absorption in the scheme. Looking then into the effects of non-linear propagation over longer distances, we determine that the steepening of the response is in fact due to the ability of the coupling field to sculpt the pulse toward a sech-shaped soliton. Over longer distances the simulations demonstrate that this probe soliton would propagate simultaneously with the resultant coupling pulse. The tendency of the pulses to separate, having different velocities due to the distinct absorption strengths of the transitions, is overcome by pulse locking.

Notably, the area theorem as applied to multtons allows the propagation even of a weak probe field in this scheme through media it would ordinarily find opaque. Our simulations of weak probes here show such propagation.

In single-field SIT the field must be strong for the propagation of solitons to overcome the weak non-linearity of the medium. But combining this approach with the CPT effect as described here suggests a way around this, and a novel approach to achieving transparent propagation of single or few photon pulses distinct from, but related to, both SIT and EIT.

It should be stressed that the results of the thin cell experiment show the nascent formation of solitons in the cw probe, but for conclusive evidence of multton propagation further investigation is required over longer distances. Balancing the requirement of low collision dephasing widths and high optical depth required may be difficult but we suggest is certainly worth attempting.

Theoretically, for modelling few photon propagation we might wish to look at a quantised field method. An interesting development of the scheme might be in coupling to Rydberg states to introduce interactions between multtons, with applications in quantum information processing.³⁹⁻⁴¹

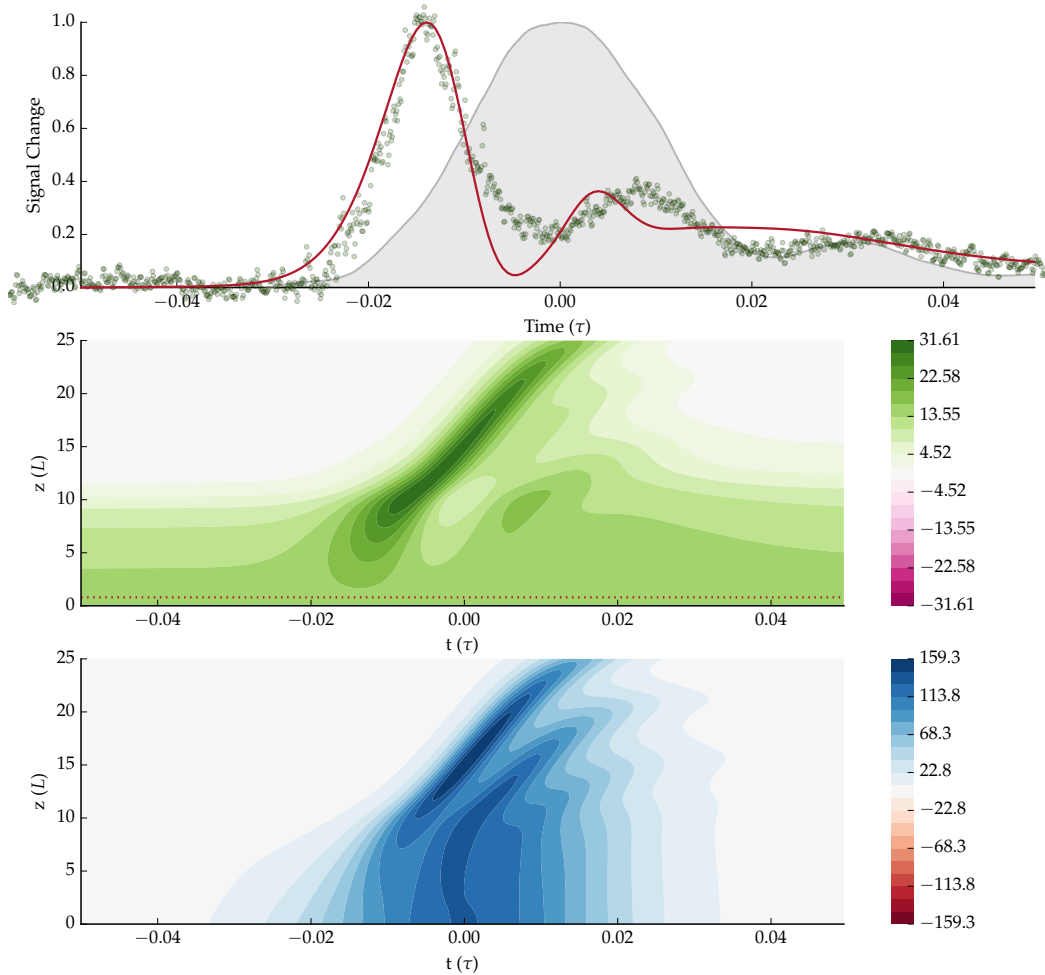


FIGURE 6.17 (Top) Comparison of numerical results (red) with experimental data (blue circles) for the normalised transmitted probe signal. The measured coupling pulse signal (grey filled area) has a width $\tau_w = 0.80\text{ ns} \equiv 0.029\Gamma_\tau$ in each case. The temperature is 230°C . (Middle) Colour map of the real part of the complex Rabi frequency for the probe field. The red dotted line marks $z = 1L$. (Bottom) Colour map of the real part of the complex Rabi frequency for the coupling pulse.

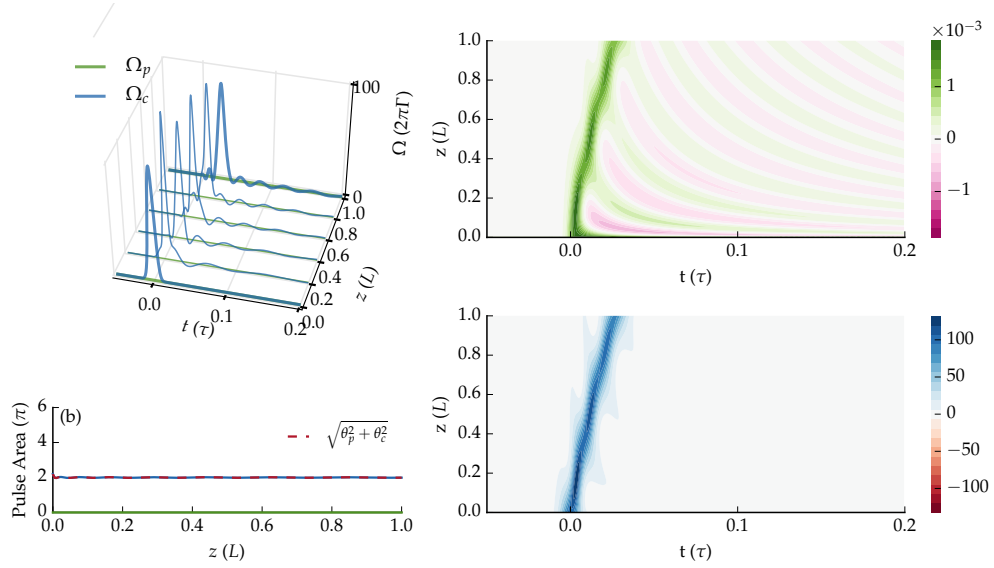


FIGURE 6.18 Propagation of a 2.2π Gaussian input coupling pulse with width 0.01τ through the V-type medium addressed by a weak $\Omega_p = 0.001\Gamma$ cw probe field. The number density is such that $N_g = 2\pi 10^3 \Gamma/L$. (Top left) Propagation profile of the probe (green) and coupling (blue) fields. (Bottom left) Pulse areas of the fields and the total area (red dashed). (Right) Colourmaps of the real part of the complex Rabi frequencies Ω_p and Ω_c .

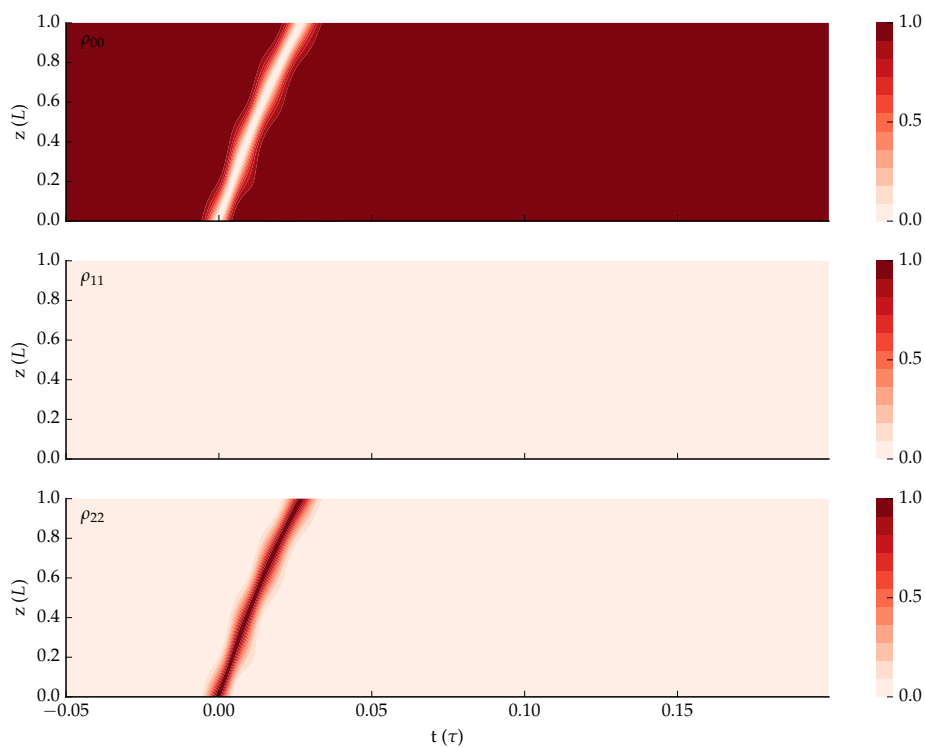


FIGURE 6.19 Populations of the ground state (top) ρ_{00} and excited states ρ_{11} (middle) and ρ_{22} (bottom) over z and t during the 0.01τ through the V-type medium addressed by a weak $\Omega_p = 0.001\Gamma$ cw probe field, as shown in figure 6.18.

7 *Conclusions*

A Dynamics of Open Quantum Systems

A.1 The Density Operator

We typically describe the state of a quantised atomic system via its state vector

$$|\psi\rangle = \sum_j c_j |j\rangle, \quad (\text{A.1})$$

a linear superposition of the eigenstates $|j\rangle$. There are many physical situations, however, in which there is significant coupling to an external environment the state evolution of which we cannot follow.

Atom-light interactions are one such system. While the processes of absorption and stimulated emission (of photons from and to the applied field) can be described within a *closed quantum system*, the process of spontaneous decay due to interaction with vacuum fluctuations surrounding an atom cannot.

For such *open quantum systems* it is useful to generalise the concept of $|\psi\rangle$ to that of the *density operator* ρ . A *pure state* is one that can be represented by a linear superposition as in (A.1), for which the density matrix is defined as $\rho = |\psi\rangle\langle\psi|$. This is clearly equivalent in information to $|\psi\rangle$. The usefulness of the density operator ρ is that it can be generalised in a

statistical way to represent incoherent superpositions of wavefunctions. We assume we have a mixture of states $|\psi_s\rangle$ each with different expansions in the eigenbasis $|j\rangle$, contained in the ensemble with probabilities $P(s) \geq 0$. The density operator for this general *mixed state* is then defined as

$$\rho = \sum_s P(s) |\psi_s\rangle \langle \psi_s| \quad (\text{A.2})$$

where for proper normalisation

$$\sum_s P(s) = 1. \quad (\text{A.3})$$

We may consider that $|\psi\rangle$ describes the intrinsic Heisenberg uncertainty required by quantum mechanics, where ρ is also able to describe additional uncertainty representing our state of knowledge of the system.⁴²

The matrix representation of the density operator in a particular basis is also known as the density matrix. The off-diagonal elements $\rho_{jk} = \langle j | \rho | k \rangle$ depend on relative phase of the coefficients and are known as *coherences*. The diagonal matrix elements $\rho_{jj} = \langle j | \rho | j \rangle$ represent the probability of a measurement finding the system in state $|j\rangle$ and are known as *populations*. These populations form a probability distribution and so must be normalised such that

$$\text{Tr} [\rho] = \sum_j \rho_{jj} = 1. \quad (\text{A.4})$$

The expectation value of an operator A in the density matrix formalism is given by

$$\langle A \rangle = \text{Tr} [A \rho]. \quad (\text{A.5})$$

A.2 The Master Equation

By substituting the density operator ρ into the standard Schrödinger equation for motion of the quantum state

$$i\hbar \frac{\partial}{\partial t} |\psi\rangle = \mathcal{H} |\psi\rangle$$

we obtain the *von Neumann equation* for unitary evolution

$$i\hbar \frac{\partial \rho}{\partial t} = [\mathcal{H}, \rho] \quad (\text{A.6})$$

which for pure states is equivalent to the Schrödinger equation.

We wish to extend the formalism to mixed states and derive an equation of motion for the open quantum system interacting with an environment. The observed effect of interaction with an unmonitored environment is to introduce non-deterministic transitions between eigenstates and dephasing between them.

We start by expanding the model to include the environment, such that the total system is closed and described by (A.6). In order to meet this requirement, we must consider the Hilbert space of the total system, and a total Hamiltonian operating over that space

$$\mathcal{H}_\Sigma = \mathcal{H} + \mathcal{H}_E + \mathcal{H}_C \quad (\text{A.7})$$

where \mathcal{H} is the Hamiltonian of the system, \mathcal{H}_E is the Hamiltonian of the environment, and \mathcal{H}_C is the Hamiltonian describing the interaction between the system and the environment.

As we're only concerned with the dynamics of \mathcal{H} , we then make a partial trace over the environment degrees of freedom in (A.6) to obtain a master equation for time evolution of the system. The *Lindblad master equation* is a general, trace-preserving and positive form for the reduced density matrix ρ , given by

$$i\hbar \frac{\partial \rho}{\partial t} = [\mathcal{H}, \rho] + \mathcal{L} \{\rho\} \quad (\text{A.8})$$

where the Lindblad term given by

$$\mathcal{L}\{\rho\} = \sum_j C_j \rho C_j^\dagger - \frac{1}{2} \left(\rho C_j^\dagger C_j + C_j^\dagger C_j \rho \right) \quad (\text{A.9})$$

is a superoperator describing the system interaction with its environment via collapse operators C_j coupling states. For example, to account for a stochastic interaction with the environment representing the decay of a system from state $|k\rangle$ to state $|j\rangle$ with rate Γ_{jk} , we include a collapse operator

$$C_j = \sqrt{\Gamma_{jk}} |j\rangle \langle k|$$

in the Linblad term.

For the Lindblad equation (A.8) to be applicable as a master equation for the system, a couple of approximations must be justified. Firstly, the Born approximation requires that the environment is sufficiently large that it is not much affected by interaction with the system. We may write this as

$$\rho_\Sigma \approx \rho \otimes \rho_E. \quad (\text{A.10})$$

Secondly, the Markov approximation requires that the time evolution depends on $\rho(t)$ and not any past history — this is also called a ‘short-memory environment’.

*B Numerical Integration of the
Lindblad Master Equation for
Large Density Matrices*

C Numerical Integration of the Maxwell-Bloch Equations

In this appendix we describe the design and implementation of numerical methods to solve the coupled Maxwell-Bloch (MB) equations describing the nonlinear propagation of near-resonant light through thermal atomic vapours. The derivation of the MB equations is given in chapter 2 and simulated results from the scheme here described are presented throughout the thesis.

C.1 Formulating the Problem

The MB equations are together equations (2.47) and (2.29), which we will restate here for completeness. They are the first-order Maxwell wave equation with the slowly-varying envelope approximation

$$\frac{\partial}{\partial z} \mathcal{E}(z, t') = i \frac{k}{2\epsilon_0} N(z) \sum_{i \neq j} d_{ij} \int_{-\infty}^{\infty} \rho_{ij}(z, t; v) f(v) dv.$$

describing propagation of the field envelope and the Lindblad master equation

$$i\hbar \frac{\partial \rho}{\partial t} = [\mathcal{H}, \rho] + \mathcal{L}\{\rho\}$$

describing the time-evolution of the atomic density matrix interacting with that field.

We describe the problem in the natural unit system defined in section ??, in terms of the length of the medium L , the natural linewidth of the transition Γ (specifically the probe transition in the case of schemes with multiple field modes) and its reciprocal natural decay time $\tau = 1/\Gamma$. Our goal is to solve the MB equations over a domain in 1D space $z \in [0, 1]$ and co-moving time $t' \in [t_{\min}, t_{\max}]$.

We begin by setting up a discrete lattice over z and t' , with N_z equal spacesteps of length $h_z = 1/N_z$, such that $z_j = j \cdot h_z \forall j \in \{0, 1, 2, \dots, N_z\}$ and N_t equal timesteps of duration $h_t = 1/N_t$, such that $t_k = k \cdot h_t \forall k \in \{0, 1, 2, \dots, N_t\}$.

The overall strategy is then to calculate values for the discretised electric field $\mathcal{E}_{j,k}$ across the lattice, for which we must determine the macroscopic polarisation $\mathcal{P}_{j,k}$ of the atoms, which in turn is derived from the density matrix $\rho_{j,k}$. A self-consistent algorithm is required for computation. Note that the electric field and polarisation envelopes in general consist of multiple modes, representing polarisations and wavelengths resonant with different transitions. For clarity in describing the scheme we will present only a single mode $\mathcal{E}_{j,k}$, but describe how the algorithm is extended to multiple modes later on.

We define a discrete set of detunings $\{\Delta_l\}$, representing atoms across a range of Doppler-shifted velocity classes. This range should be broad enough to cover the Maxwell-Boltzmann probability distribution and dense enough to accurately map the spectral absorption window. We will discuss those accuracy requirements in section C.3.

Any formulation of an integration scheme for partial differential equations is complete only with the definition of appropriate boundary conditions. Here we take a boundary condition for the field at the front of the medium (*i.e.* $j = 0$) defining the field profile over time input on the medium $\mathcal{E}_{j=0,k}$. In a typical simulation of experiment this might be a

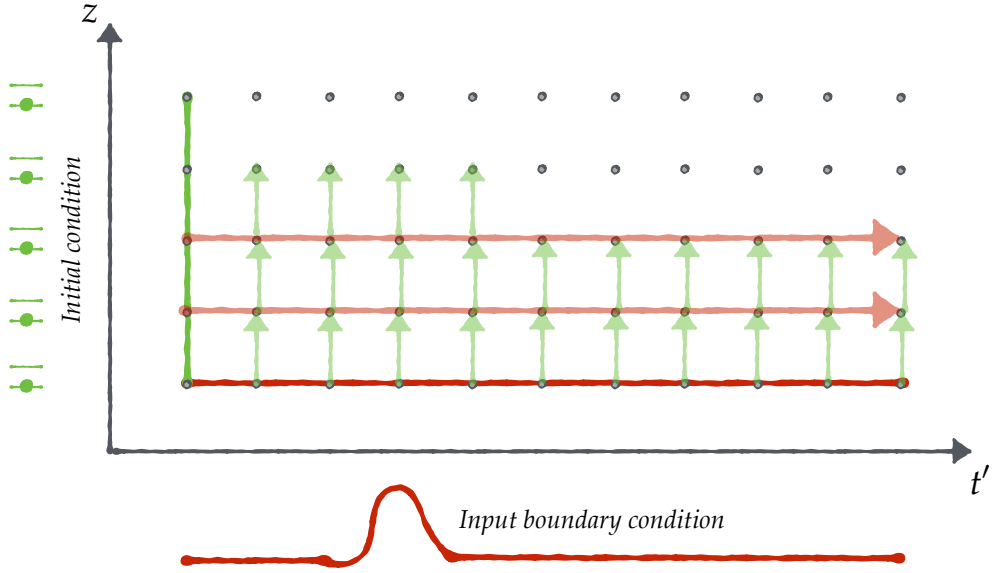


FIGURE C.1 Finite difference integration scheme for the Maxwell-Bloch equations.

The equations are solved for a discrete lattice over space z and co-moving time t' . At each lattice point (z_j, t'_k) we wish to solve for the electric field $\mathcal{E}(z_j, t'_k)$ and the atomic density matrix $\rho(z_j, t'_k)$. The initial condition is illustrated by the two-level icons on the left. The boundary condition defining the electric field pulse profile over time input on the medium is illustrated by the sketched pulse at the bottom.

pulse or a ramp-on to a cw field. We must also specify an initial condition for the density matrix $\rho_{j,k=0}$. Typically we set this such that all population starts off in the atomic ground state.

C.2 Computational Scheme

The finite difference scheme is illustrated in figure C.1 and sketched out with pseudocode in algorithm 1. For each spacestep index j in the medium, we take the field $\mathcal{E}_{j,k}$ arriving on that step for all timesteps t'_k . For the first spacestep ($j = 0$) this is the input boundary condition, il-

Algorithm 1 Maxwell-Bloch integration.

```

1: for  $j = 2$  to  $N_z$  do                                 $\triangleright$  Loop over spacesteps
2:   for  $l = 0$  to  $N_\Delta$  do                       $\triangleright$  Loop over velocity classes
3:      $\rho_j^l = \text{solve\_lindblad}(\rho_{\text{init}}, \mathcal{E}_j, \Delta_l)$ 
4:   end for
5:   for  $k = 0$  to  $N_t$  do                       $\triangleright$  Loop over timesteps
6:      $\mathcal{P}_{j,k} = \mathcal{N}_z \sum_{a \neq b} \int_l d_{ab} \rho_{j,k}^l [a, b] f(\Delta_l, u) d\Delta$ 
7:      $\mathcal{E}_{j+1,k} = \mathcal{E}_{j+1,k} + i h_z \frac{k}{2\varepsilon_0} \left[ \frac{3}{2} \mathcal{P}_{j,k} - \frac{1}{2} \mathcal{P}_{j-1,k} \right]$        $\triangleright$  The AB step
8:   end for
9: end for

```

lustrated in red in figure C.1. Next (lines 2–4 in the pseudocode) we loop over the velocity classes l and pass the detuning Δ_l , the field profile $\mathcal{E}_{j,k}$ and an initial condition (ρ_{init}) to the Lindblad solver described in Appendix B. That solver contains an implicit loop through the N_t timesteps, and integrates the Lindblad equation to find the density matrix at each of those timesteps t_k' .

At this point we have solved for the density matrix ρ_j^l at the spacestep z_j for each time t_k and for atoms in each velocity class l . In a loop over the timestep index k (lines 5–8) we then perform an average of the density matrix coherences over detuning, weighted by the Maxwell-Boltzmann probability distribution for a defined width u , and sum them to find (line 6) the polarisation $\mathcal{P}_{j,k}$ at that point in space z_j and time t_k .

Once we have computed the polarisation, and still within the loop over timesteps, we can advance the field at that timestep to the next spacestep $\mathcal{E}_{j+1,k}$ in the medium for each k using a second-order Adams-Bashforth method. Note then that this method is not strictly chronological, but is self-consistent in the co-moving frame of reference.

C.2.1 Details of the Algorithm

The pseudocode above describes the general calculation scheme, but omits a number of details that we will now describe.

First, we have considered only a single field mode. For multiple modes, we must input all of those modes to the Lindblad solver (in line 3). We must also calculate polarisations for each mode separately from its coupled transitions (line 6) and advance the fields for each mode (line 7).

Second, note that we started the spacestep loop (line 1) at $j=2$. The two-step Adams-Bashforth method requires two starting points to begin. We therefore use an explicit Euler step to take the input field at $j=0$ to the next step at $j=1$. As the local error in the Euler step is of order $\mathcal{O}(h_z)$, we use a smaller step to avoid introducing a large global error. The second step is then a two-step Adams-Bashforth with different stepsizes.

The correct difference formula for this step (D.6) is derived in Appendix D. The remaining steps use the standard two-step Adams-Bashforth step as shown in the pseudocode.

Third, the Lindblad solver (line 3) requires the electric field envelope \mathcal{E}_j to be passed as a function of time, rather than an array, as the adaptive method may choose different inner stepsizes (*i.e.* steps between t'_k and t'_{k+1} for any k) that we do not know in advance. We construct this function for arbitrary points in the time domain using quadratic spline interpolation.^{43,44}

Fourth, the complex values for the field envelopes $\mathcal{E}_{j,k}$ and atomic density matrix $\rho_{j,k}$ across the lattice is saved to disc in binary format, such that the results of each simulation can be loaded without needing the calculation to be repeated. To optimise storage and memory requirements, a data resolution in z_h and t_k may be specified, sufficient for analysis and visualisation without needing to record all of the steps that

may be required for stability and accuracy.

Spectral analysis of the results is performed using a discrete Fourier transform of the complex field.⁴³

C.2.2 Code Implementation

The algorithm for solving the MB equations was implemented in Python using the SciPy scientific computing stack.^{45,46}

The code uses the OB class of the OpticalBloch package described in appendix B in order to define the atom-light interaction and solve the Lindblad equation for instances representing various atomic systems, with few-level or with full angular momentum structure. The QuTiP library⁴⁷ is used for quantum state and operator objects and its master equation solver for dynamics of open quantum systems.

C.3 Convergence & Accuracy

We check the accuracy of the method with a quantitative measurement of the convergence of results for a particular system with increased number of spacesteps and velocity classes. We wish the results to be as accurate as possible, but with an awareness of the trade-off that the computational complexity (and thus running time) scales with $\mathcal{O}(N_z)$ and $\mathcal{O}(N_\Delta)$ where N_Δ is the number of velocity classes.

In figure C.2 we show the results of convergence of the integrated solutions for different numbers of spacesteps N_z between 10 and 500. The convergence is measured relative to a benchmark at 10,000 spacesteps — a number which ensures high accuracy but is too slow for performing many calculations. The maximum value of the absolute difference

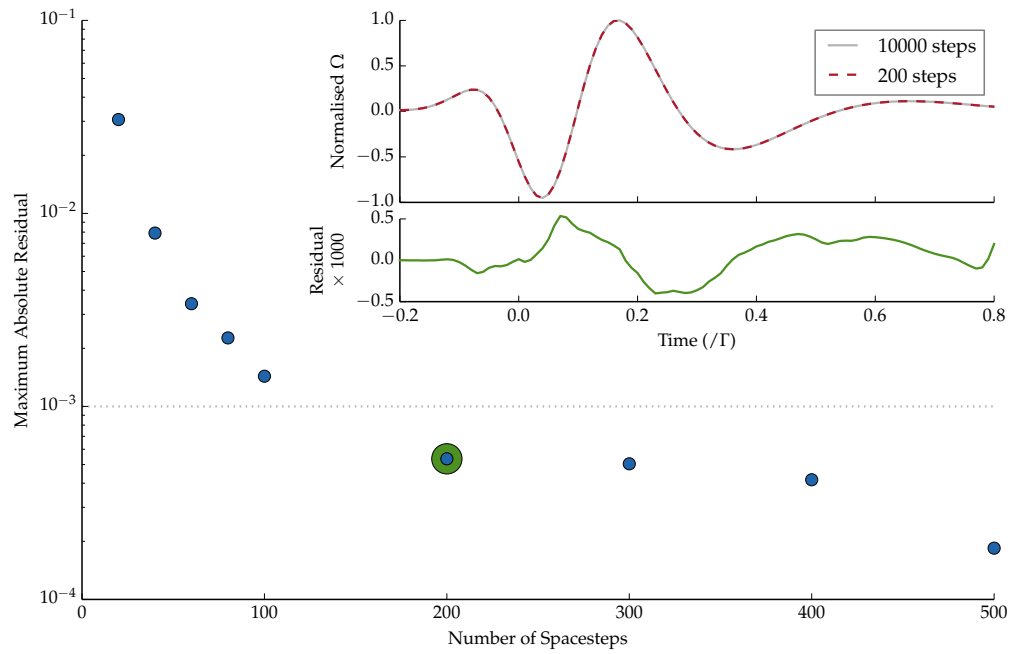


FIGURE C.2 Convergence of an example integrated solution, for a weak pulse in a medium with $\mathcal{N}g = 2\pi 100$ MHz, for different numbers of spacesteps N_z . (Main plot) The minimum absolute residual between an integrated solution N_z and a benchmark solution with 10,000 steps (blue circles), plotted on a logarithmic y -axis. The dotted line represents a chosen accuracy requirement of 10^{-3} and the green circled data point is the lowest number of steps tested which meets this requirement, in this case $N_z = 200$. (Inset) Normalised Ω against time at the final spacetime step $j = N_z$ for both the benchmark and the $N_z = 200$ run, with the residual shown underneath.

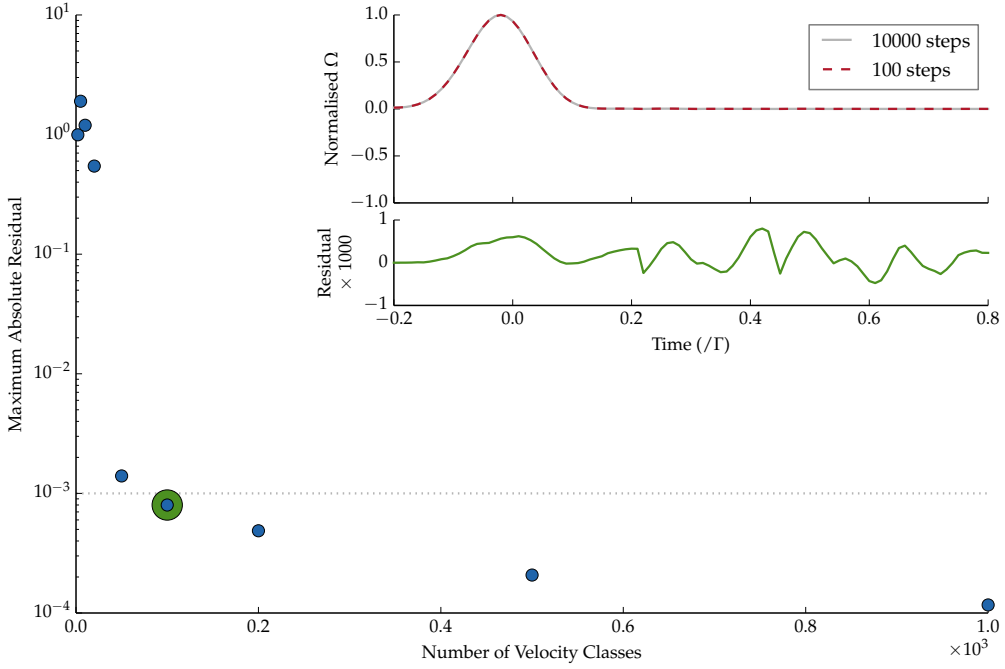


FIGURE C.3 Convergence of an example integrated solution, for a weak pulse in a medium with $\mathcal{N}g = 2\pi 100 \Gamma/\text{L}$ and a thermal width of $2\pi 10 \Gamma$, for different numbers of velocity classes N_Δ . (Main plot) The minimum absolute residual between an integrated solution N_Δ and a benchmark solution with 10,000 velocity classes, plotted on a logarithmic y -axis. The dotted line represents a chosen accuracy requirement of 10^{-3} and the green circled data point is the lowest number of steps tested which meets this requirement, in this case $N_\Delta = 100$. (Inset) Normalised Ω against time at the final spacestep $j = N_j$ for both the benchmark and the $N_\Delta = 100$ run, with the residual shown underneath.

(residual) between the benchmark and each run is plotted. We see that the maximum absolute residual decreases with the number of steps N_z down to 200 steps, after which the increase in accuracy for an increased number of steps is reduced. If we choose a tolerance for the maximum absolute residual of 10^{-3} (shown by the dotted line), the first tested run within that tolerance is $N_z = 200$. Running simulations with this number of spacesteps would therefore reduce calculation many times over the benchmark while keeping a sufficient level of accuracy.

In figure C.3 we show a similar figure for results of convergence for the integrated solutions for different numbers of velocity classes N_Δ between 1 and 1,000 spread over a width of $2\pi 40\Gamma$.

The convergence is measured relative to a benchmark at 10,000 velocity classes. We see that the maximum absolute residual is large for few velocity classes, around 1. If we again choose a tolerance for the maximum absolute residual of 10^{-3} (shown by the dotted line), the first tested run within that tolerance is $N_z = 100$. The ‘return on investment’ for additional velocity classes is reduced from then on, with $N_z = 1,000$ not providing an order of magnitude improvement in accuracy.

In picking a range of velocity classes for an accurate simulation, there are two important considerations. First, it is important to cover the Maxwell- Boltzmann distribution. We check the integration width is sufficient by using a simple trapezoidal integration over the discrete Maxwell-Boltzmann distribution to ensure it is close to unity. In each of the calculations above we used an evenly-spaced sampling over four times the FWHM. The integral is far from unity until around 20 detuning steps (when it reaches 0.995), which explains why we don’t see convergence in the first few samples. Second, it is important to sample accurately the Lorentzian resonance window, which is typically much smaller than the thermal width (in our case it is specified to be $2\pi 1\Gamma$). In order to achieve both of these goals with an optimised number of detuning steps, we use a non-evenly spaced grid with a denser number of velocity classes around resonance, which can improve accuracy without requiring as many velocity classes.

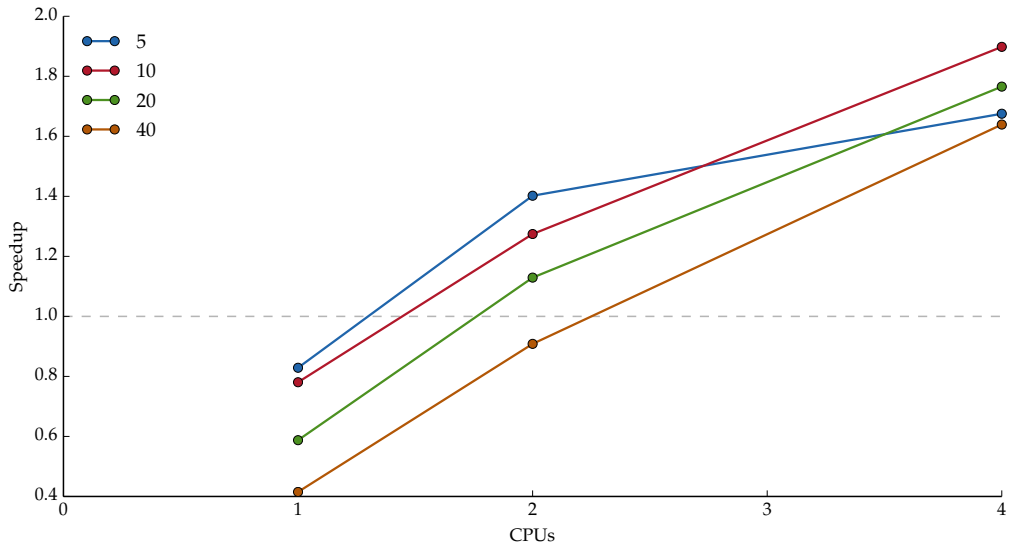


FIGURE C.4 Speedup of parallelised computation versus number of CPUs for different numbers of velocity classes $N_{\Delta} = \{5, 10, 20, 40\}$, relative to the serial algorithm. Each data point is ‘best of two’ to avoid times where the CPUs might otherwise be used by the operating system.

C.4 Parallelisation & Performance

The pseudocode in algorithm 1 contains a number of nested loops, which leads us to consider if any parts of the implementation may readily be parallelised.

The iterations of the outermost loop over space steps z_j (algorithm 1, line 1) are not independent (*i.e.* the field at a point in space j is dependent on the previous space points $0, 1, \dots, j - 1$) which necessitates that these be processed in serial. However, the iterations of the inner loop over velocity classes Δ_l (algorithm 1, line 2), calculate the evolution of atoms subject to different Doppler shifts with respect to the fields along z . The evolution of each class is completely independent of the others so these may be processed in parallel, with the weighted average calculated at the end.

In figure C.4 we present measured speedup of parallelised computation with increasing number of CPU for example simulations using 5, 10, 20 and 40 velocity classes, relative to the serial code.

We see that, for all numbers of velocity classes tested, using the parallel code but only allowing use of a single CPU incurs a slowdown due to the overhead of passing objects into the parallelised functions.

In general the speedup decreases with the number of velocity classes, which indicates that there is significant overhead in parallelisation. With 2 CPUs we have speedup up to the case of 20 velocity classes. With 4 CPUs, the parallel algorithm results in significant speedup, above 60% in each case. The speedup for 5 velocity classes with 4 CPUs or more is obviously limited.

The Lindblad solver routine in the velocity class loop represents the most computationally-intensive part of the whole algorithm, so it is certainly useful to be able to make use of multiple core computers to perform these calculations. For the work described in this thesis we made use of an Intel Core i7 with up to 4 CPU cores, and for the most intensive calculations we used Durham University's *Hamilton* HPC Cluster with up to 12 CPU cores for each simulation.

Another process which could be computed in parallel is the iteration over timesteps t_k (algorithm 1, line 7), which performs the weighted average over density matrix coherences to determine the polarisation of the medium at that time, and advances the field via the AB step. However, for the number of timesteps used in calculations we saw negligible speedup due to the high overhead required for this loop in passing arrays containing the polarisations and fields. In fact, for systems where less than $N_k = 1000$ timesteps are required for the necessary accuracy, this overhead caused the parallel implementation to be slower than the serial. It was therefore not used.

For fields with many modes, loops over these modes could be parallelised for computing polarisation. In this work we have only needed to consider systems of one or few modes, so it was not appropriate to implement parallelisation here.

D The Two-Step Adams-Bashforth Method with Varying Stepsize

Adams-Bashforth integration methods have a well-known derivation but we are not aware of a reference for the two-step method in the case that the two stepsizes are different, so we present the result here. This numerical method is used in solving the MB equations as described in chapterC. The two-step method requires two initial points, and the second point is calculated using a Euler step, which we wish to keep small to avoid introducing a large global error. The third point is then calculated with the Adams-Bashforth method with different step sizes. From then on the standard Adams-Bashforth method can be used.

We take an ordinary differential equation $y' = f(z, y(z))$ with an initial condition $y(z_0) = y_0$ that we wish to solve numerically. If we know $y(z)$ at a time z_n and want to know what z is at a later time z_{n+1} , the fundamental theorem of calculus tells us that we find it by integrating y' over the time interval

$$y(z_{n+1}) = y(z_n) + \int_{z_n}^{z_{n+1}} y'(z) dz = y(z_n) + \int_{z_n}^{z_{n+1}} f(z, y(z)) dz. \quad (\text{D.1})$$

The idea behind any ODE integrator is to compute the right-hand-side integral for some numerical approximation of f . The problem is then computed over a series of steps $n = 1, 2, \dots, N$ to give a sequence of points z_n which approximate $y(z)$ to some order of accuracy as a func-

tion of the stepsize. The method is consistent if the local error (*i.e.* the error from step n to step $n + 1$) goes to zero faster than the stepsize $(z_{n+1} - z_n)$ goes to zero.

Where the Euler method takes the slope f to be a constant on the interval $[z_n, z_{n+1}]$, the idea behind Adams-Bashforth methods is to approximate f by a Lagrange interpolating polynomial⁴⁸

$$P(z) = \sum_{j=1}^m P_j(z) \quad (\text{D.2})$$

where

$$P_j(z) = y_j \prod_{\substack{k=1 \\ k \neq j}}^m \frac{z - z_k}{z_j - z_k}. \quad (\text{D.3})$$

Here $P(z)$ is the polynomial of degree $\leq (m - 1)$ that passes through the m points $(z_1, y_1 = f(z_1)), (z_2, y_2 = f(z_2)) \dots (z_m, y_m = f(z_m))$. We'll take the linear ($m = 2$) interpolant on the point z_n and an earlier point z_{n-1} , so we have

$$P(z) = f(z_n, y_n) \frac{z - z_{n-1}}{z_n - z_{n-1}} + f(z_{n-1}, y_{n-1}) \frac{z - z_n}{z_{n-1} - z_n}. \quad (\text{D.4})$$

Now if we substitute this approximating polynomial into the integral in (D.1), we find

$$\begin{aligned} \int_{z_n}^{z_{n+1}} f(z, y(z)) dz &\approx \int_{z_n}^{z_{n+1}} P(z) dz \\ &= \int_{z_n}^{z_{n+1}} \left[f(z_n, y_n) \frac{z - z_{n-1}}{z_n - z_{n-1}} + f(z_{n-1}, y_{n-1}) \frac{z - z_n}{z_{n-1} - z_n} \right] dz \end{aligned}$$

into which we may then put in the limits to obtain

$$\begin{aligned} \int_{z_n}^{z_{n+1}} f(z, y(z)) dz &\approx \frac{(z_n - z_{n+1})}{2(z_{n-1} - z_n)} \left[f(z_n, y_n)(z_n + z_{n+1} - 2z_{n-1}) \right. \\ &\quad \left. - f(z_{n-1}, y_{n-1})(z_n - z_{n+1}) \right]. \quad (\text{D.5}) \end{aligned}$$

If we let $h_1 := z_n - z_{n-1}$ and $h_2 := z_{n+1} - z_n$ then

$$\int_{z_n}^{z_{n+1}} P(z) dz = \frac{h_2}{2h_1} [(2h_1 + h_2)f(z_n, y_n) - h_2 f(z_{n-1}, y_{n-1})].$$

Putting this back into the approximation of (D.1), we get

$$y(z_{n+1}) \approx y(z_n) + \frac{h_2}{2h_1} [(2h_1 + h_2)f(z_n, y_n) - h_2 f(z_{n-1}, y_{n-1})]$$

and our sequence of approximation points y_n is calculated as

$$y_{n+1} = y_n + \frac{h_2}{2h_1} [(2h_1 + h_2)f(z_n, y_n) - h_2 f(z_{n-1}, y_{n-1})] \quad (\text{D.6})$$

for $n = 1, 2, \dots, N$. This is the correct second-order Adams-Bashforth finite difference step in the case that the stepsizes are different.

If the steps are of equal size, i.e. $h := h_1 = h_2$ we find

$$y_{n+1} = y_n + \frac{3}{2}hf(z_n, y_n) - \frac{1}{2}hf(z_{n-1}, y_{n-1}) \quad (\text{D.7})$$

which is the standard two-step Adams-Bashforth method.^{49,50}

Acknowledgements

I would like to thank...

Bibliography

- ¹ J D Jackson. *Classical Electrodynamics*. Wiley, 1998.
- ² R W Boyd. *Nonlinear Optics*. Nonlinear Optics Series. Elsevier Science, 2008.
- ³ E Hecht. *Optics*. Pearson Education, 2015.
- ⁴ P Lambropoulos and D Petrosyan. *Fundamentals of Quantum Optics and Quantum Information*. Springer, 2007.
- ⁵ D J Griffiths. *Introduction to Electrodynamics*. Prentice Hall, 1999.
- ⁶ Mary B. James. Why the speed of light is reduced in a transparent medium, 1992.
- ⁷ R P Feynman, R B Leighton, and M L Sands. *The Feynman Lectures on Physics*. Number v. 1 in The Feynman Lectures on Physics. Addison-Wesley, 1963.
- ⁸ B H Bransden and C J Joachain. *Physics of Atoms and Molecules*. Pearson Education. Prentice Hall, 2003.
- ⁹ G Grynberg, A Aspect, C Fabre, and C Cohen-Tannoudji. *Introduction to Quantum Optics: From the Semi-classical Approach to Quantized Light*. Cambridge University Press, 2010.

- ¹⁰ C Cohen-Tannoudji, J Dupont-Roc, and G Grynberg. *Atom-photon interactions: basic processes and applications*. Wiley-Interscience publication. J. Wiley, 1992.
- ¹¹ Charles S. Adams and Erling Riis. Laser Cooling and Manipulation of Neutral Particles. pages 1–39, 1997.
- ¹² A. Icsevgi and W. E. Lamb. Propagation of light pulses in a laser amplifier. 1429, 1964.
- ¹³ C J Foot. *Atomic physics*. Oxford master series in physics. Oxford University Press, 2005.
- ¹⁴ J. Gea-Banacloche, Yong-qing Li, Shao-zheng Jin, and Min Xiao. Electromagnetically induced transparency in ladder-type inhomogeneously broadened media: Theory and experiment. *Physical Review A*, 51(1):576, 1995.
- ¹⁵ R Loudon. *The Quantum Theory of Light*. OUP Oxford, 2000.
- ¹⁶ L Allen and J H Eberly. *Optical Resonance and Two-level Atoms*. Dover books on physics and chemistry. Dover, 1975.
- ¹⁷ a. V. Durrant. Some basic properties of stimulated and spontaneous emission: A semiclassical approach. *American Journal of Physics*, 44(7):630, 1976.
- ¹⁸ Edwin Hewitt and Robert E. Hewitt. The Gibbs-Wilbraham phenomenon: An episode in fourier analysis. *Archive for History of Exact Sciences*, 21(2):129–160, 1979.
- ¹⁹ Paul Siddons, Charles S. Adams, Chang Ge, and Ifan G. Hughes. Absolute absorption on rubidium D lines: comparison between theory and experiment. *Journal of Physics B: Atomic, Molecular and Optical Physics*, 41(15):155004, aug 2008.

- ²⁰ James Keaveney. *Cooperative interactions in dense thermal Rb vapour confined in nm-scale cells*. PhD thesis, 2013.
- ²¹ B. Huber, T. Baluktsian, M. Schlagmüller, a. Kölle, H. Kübler, R. Löw, and T. Pfau. GHz Rabi flopping to Rydberg states in hot atomic vapor cells. *Physical Review Letters*, 107(24):1–4, 2011.
- ²² T. Baluktsian, B. Huber, R. Löw, and T. Pfau. Evidence for strong van der Waals type Rydberg-Rydberg interaction in a thermal vapor. *Physical Review Letters*, 110(12):1–4, 2013.
- ²³ Ennio Arimondo, M. Inguscio, and P. Violino. Experimental determinations of the hyperfine structure in the alkali atoms. *Reviews of Modern Physics*, 49(1):31–75, 1977.
- ²⁴ A Banerjee, D Das, and V Natarajan. Absolute frequency measurements of the D1 lines in ^{39}K , ^{85}Rb , and ^{87}Rb with ~ 0.1 ppb uncertainty, 2007.
- ²⁵ James Keaveney, Ifan G. Hughes, a. Sargsyan, D. Sarkisyan, and Charles S. Adams. Maximal Refraction and Superluminal Propagation in a Gaseous Nanolayer. *Physical Review Letters*, 109(23):233001, dec 2012.
- ²⁶ D V Schroeder. *An Introduction to Thermal Physics*. Addison Wesley, 2000.
- ²⁷ E.L. Lewis. Collisional relaxation of atomic excited states, line broadening and interatomic interactions, 1980.
- ²⁸ A Thorne, U Litzén, and S Johansson. *Spectrophysics: Principles and Applications*. Springer, 1999.
- ²⁹ Lee Weller, Robert J Bettles, Paul Siddons, Charles S. Adams, and Ifan G. Hughes. Absolute absorption on the rubidium D 1 line in-

- cluding resonant dipole-dipole interactions. *Journal of Physics B: Atomic, Molecular and Optical Physics*, 44(19):195006, oct 2011.
- ³⁰ K. Razdan. Demonstrating optical saturation and velocity selection in rubidium vapor. *American Journal of Physics*, 67(9):832, 1999.
- ³¹ Kang Bin Im, Hye Yun Jung, Cha Hwan Oh, Seok Ho Song, Pill Soo Kim, and Ho Seong Lee. Saturated absorption signals for the Cs D₂ line. *Physical Review A - Atomic, Molecular, and Optical Physics*, 63(3):1–4, 2001.
- ³² S Nakayama. Theoretical analysis of Rb and Cs D₂ lines in Doppler-free spectroscopic techniques with optical pumping. *Japanese Journal of Applied Physics*, 24(1):1–7, 1985.
- ³³ David a. Smith and Ifan G. Hughes. The role of hyperfine pumping in multilevel systems exhibiting saturated absorption. *American Journal of Physics*, 72(5):631, 2004.
- ³⁴ Ben E. Sherlock and Ifan G. Hughes. How weak is a weak probe in laser spectroscopy? *American Journal of Physics*, 77(2):111, 2009.
- ³⁵ Daniel Adam Steck. Rubidium 87 D line data. 2001.
- ³⁶ V.R. Blok and G.M. Krochik. Lasing Without Inversion. *Digest on Nonlinear Optics: Materials, Phenomena and Devices*, 7, 1990.
- ³⁷ Michael Fleischhauer, Atac Imamoglu, and Jonathan P Marangos. Electromagnetically induced transparency : Optics in coherent media. *Reviews of Modern Physics*, 77(2):633–673, 2005.
- ³⁸ Robert Potvliege. No Title. personal communication.
- ³⁹ Daniel T Maxwell, D. J. Szwer, D. Paredes-Barato, H. Busche, Jonathan D Pritchard, A. Gauguet, Kevin J. Weatherill, M. P. a. Jones,

- and Charles S. Adams. Storage and Control of Optical Photons Using Rydberg Polaritons. *Physical Review Letters*, 110(10):103001, mar 2013.
- ⁴⁰ Mark Saffman, Thad G Walker, and Klaus Mølmer. Quantum information with Rydberg atoms. *Reviews of Modern Physics*, 82(3):2313–2363, aug 2010.
- ⁴¹ M. F. Maghrebi, M. J. Gullans, P. Bienias, S. Choi, I. Martin, O. Firstenberg, M. D. Lukin, H. P. Büchler, and a. V. Gorshkov. Coulomb bound states of strongly interacting photons. *Phys. Rev. Lett.*, 115(September):123601, 2015.
- ⁴² Daniel Adam Steck. Quantum and Atom Optics. page 932, 2007.
- ⁴³ W H Press. *Numerical Recipes 3rd Edition: The Art of Scientific Computing*. Cambridge University Press, 2007.
- ⁴⁴ C. De Boor. On calculating with B-splines. *Journal of Approximation Theory*, 6(1):50–62, 1972.
- ⁴⁵ Stéfan Van Der Walt, S. Chris Colbert, and Gaël Varoquaux. The NumPy array: A structure for efficient numerical computation. *Computing in Science and Engineering*, 13(2):22–30, 2011.
- ⁴⁶ Eric Jones, Travis Oliphant, Pearu Peterson, and Others. {SciPy}: Open source scientific tools for {Python}.
- ⁴⁷ P D Nation and J R Johansson. QuTiP : The Quantum Toolbox in Python. 2013.
- ⁴⁸ G B Arfken and H J Weber. *Mathematical Methods For Physicists International Student Edition*. Elsevier Science, 2005.
- ⁴⁹ L Edsberg. *Introduction to Computation and Modeling for Differential Equations*. Wiley, 2008.

⁵⁰ Francis Bashforth and John Couch Adams. *An attempt to test the theories of capillary action: by comparing the theoretical and measured forms of drops of fluid. With an explanation of the method of integration employed in constructing the tables which give the theoretical forms of such drops.* University Press, 1883.